TÉCNICO LISBOA

Experimental and Numerical Characterization of an Ejector Pump Burner for Small Scale Firing Systems

Muhammad Ferdous Raiyan

Thesis to obtain the Master of Science Degree in

Energy Engineering and Management

Supervisor(s):   Professor Dr. Edgar Caetano Fernandes
                 Professor Dr. Miguel Abreu de Almeida Mendes

Examination Committee

Chairperson: Professor Dr. Francisco Manuel Da Silva Lemos

Supervisor(s): Professor Dr. Edgar Caetano Fernandes

Member of the Committee: Professor Dr. Aires José Pinto dos Santos

November 2019

In memory of my late maternal grandparents Mr. Abdul Wadud and Mrs. Rowshan Ara Begum and my late paternal grandfather Mr. AKM Mahbub Ullah. I'd like to dedicate also to the memory of my another grandfather (mother's uncle) Mr. Zia Uddin Ahmed. They are physically absent but their guidance and teachings will always be with me.

Acknowledgments

This work was developed at the Thermofluids, Combustion and Energy Systems laboratory of the IN+ - Center for Innovation, Technology and Policy Research.

Resumo

A presente dissertação tem como objetivo desenvolver um modelo de arrastamento de ar para um queimador com bomba de injetor onde o jato de combustível arrasta ar ambiente para uma combustão de pré-mistura, maioritariamente usada em fogões domésticos. Um estudo paramétrico numérico e experimental foi realizado para perceber o modelo de arrastamento de ar, determinando assim os fatores-chave que afetam diretamente a quantidade de ar arrastado, influenciando consequentemente a razão de equivalência . Com base em estudos de CFD, os efeitos do diâmetro do tubo (D), geometria do injetor, condições de injeção e distância entre tubo e injetor (Δ) foram analisados, sendo também caracterizados por técnicas de diagnóstico não intrusivas. Um limite ótimo foi proposto no D e após o estudo paramétrico.

A geometria real leva a um maior arrastamento de ar, com os resultados numéricos perto dos obtidos com PIV, com uma discrepância entre 3% e 6%. Já no caso ideal, a discrepância ficou entre 15% e 20%. Avaliando a razão de equivalência em CFD e espectroscopia para os diferentes casos, foram observados comportamentos semelhantes em termos de discrepância. As características do arejamento primário baseadas em simulação isotérmica e não-isotérmica foram avaliadas, com o modelo isotérmico a prever maior arejamento que o não-isotérmico. Com um modelo simples de combustão de pré-mistura e uma geometria ideal, estimou-se a libertação de calor e distribuição mássica das diferentes espécies. Os efeitos de diversos parâmetros na razão de equivalência e emissão de CO foram explorados.

Palavras-chave: Queimador de bomba ejetor, Entrada de ar, Combustão, Modelagem numérica, PIV, Espectroscopia

Abstract

The present work aims to develop an air entrainment model for ejector pump burner where fuel jet draws ambient air for a premixed combustion which is mainly used in domestic cooking stove. A detailed numerical and experimental parametric study has been performed to understand air entrainment model thus determining the key factors directly affecting the amount of air entrainment which consequently affects the equivalence ratio (ϕ). Based on CFD modeling, the effects of tube diameter (D), injector geometry, injection condition, distance between tube and injector (Δ) have been studied which are also characterized by non-intrusive diagnostic techniques. An optimum limit regarding tube size (D) and distance (Δ) have been proposed after parametric study.

Ideal and *real* geometries in CFD environment have been studied to investigate their influence on primary aeration. *Real* geometry leads to higher entrainment and the results showed close matching with PIV technique with a 3% to 6% discrepancy. While comparing to ideal case, the discrepancy remained in between 15% to 20%. Similar behavior in terms of discrepancy were obtained while evaluating equivalence ratio (ϕ) for different test cases (CFD) and comparing them to the results from spectroscopy. The primary aeration characteristics based on isothermal and non-isothermal modeling have been investigated and isothermal model predicted more aeration than non-isothermal case. A simple premixed combustion model with ideal geometry estimated the heat release and the distribution of mass fraction of different species. Effects of different parameters on equivalence ratio and CO emission have been explored from the results.

Keywords: Ejector pump burner, Air entrainment, Combustion, Numerical modeling, PIV, Spectroscopy

Contents

List of Tables

List of Figures

Nomenclature

Acronyms

C_2 Dicarbon

CH Methylidyne radical

OH Hydroxyl radical

CFD   Computational Fluid Dynamics

CO   Carbon Mono Oxide

FEM   Finite Element Method

LES   Large Eddy Simulation

LHV   Lower Heating Value [MJ/Kg]

LPG   Liquefied Petroleum Gas

NOx   Nitrogen Oxides

PIV   Particle Image Velocimetry

SLPM Standard Liters Per Minute [L/min]

SST   Shear Stress Transport

Greek symbols

ϵ Rate of dissipation of turbulence energy [$J/kg.s$]

κ Turbulent kinetic energy [J/kg]

λ Excess air ratio

μ Dynamic viscosity [$Pa.s$]

ω Specific rate of dissipation [$1/s$]

ϕ Equivalence ratio

ρ Density [kg/m^3]

τ	Viscous stress $[N/m^2]$
Δ	Distance between tube and injector $[cm]$
α_p	Thermal expansion coefficient $[1/K]$
μ_T	Eddy viscosity $[Pa.s]$

Roman symbols

C_p	Specific heat at constant pressure $[J/kg/K]$
D_k^m	Mixture averaged mass diffusion coefficient $[m^2/s]$
D	Mixing tube external diameter $[cm]$
d	Injector diameter $[mm]$
R_m	Entrainment ratio
f_k	Body forces associated with the kth species $[N]$
K	Thermal conductivity $[W/mK]$
Le_k	Lewis number
L	Mixing tube length $[cm]$
l	Injector length $[cm]$
$\dot{m}_{ae}$	Mass flow rate of entrained air $[kg/s]$
$\dot{m}_{as}$	Mass flow rate of secondary entrained air $[kg/s]$
$\dot{m}_f$	Mass flow rate of fuel $[kg/s]$
$\dot{m}_m$	Mass flow rate of air fuel mixture $[kg/s]$
$\dot{v}_{in}$	Inlet volume flow rate in SLPM $[L/min]$
M_{wi}	Molecular weight of species i $[g/mol]$
Pr	Prandtl number
t	Mixing tube thickness $[cm]$
u	Velocity vector $[m/s]$
V_k	Diffusive velocity of the kth species [m/s]
Y_k	Mass fraction of the kth species

Chapter 1

Introduction

1.1 Motivation and Fundamentals of the Topic

The journey of science and technology for modern human race started since the invention of fire. Since then, long time has been passed and many evolutionary as well as revolutionary events and inventions have been witnessed by mankind. Energy, more specifically thermal energy has become the prime mover behind all the major developments. As a result, combustion is a robust source of energy for mankind, which has the applications ranging from the most primitive to the latest inventions. No matter wherever is the focus, either in an industry or transportation as well as domestic applications and electrical energy production, today combustion is playing crucial roles.

Extensive research and development have been carried out to investigate various types of combustion with different fuels at different conditions depending on the applications. As the chemical mechanism involves complexity and requires high level of knowledge and understanding in thermodynamics depending on different conditions, there are always novel ways to thrive for the discovery of new system design and optimization for any combustion system whether it's a small cooking burning or a huge gas turbine.

Combustion can be defined as the mechanism in which the chemical energy of fuel is converted into thermal energy. Most of the combustion processes require at least two components in the reactants, which are: a fuel and an oxidant. Rearrangements of the chemical bonds in these compounds lead to the formation of "products". Three very important parameters: temperature, reactants mixing and time have strong influence on combustion [1].

Estimated three billion people around the world burn firewood, coal, dung, crop residue and charcoal in traditional stoves for cooking and heating purpose [2]. Household air pollution due to incomplete combustion of such fuels is responsible around the world for 4.3 million premature deaths per year and 1.7 million of them is in South Asia. It surpasses the burden of disease from any other energy related environmental risk factor [3, 4].

It has been found that household air pollution from traditional cooking stoves presents a greater health risk than other environmental factors. Research shows that even after government support to promote clean cooking stove, over 700 million people in South Asia will still be depending on traditional stoves

in 2030. This number may rise in case the climate change alleviation efforts increase energy costs. Fuel choice as well as stove modeling are excellent options to study depending on the fuel price, population, location as well as energy demand [5]. Thus, development of a clean and easy cooking system that improve people's quality of life (QOL) is not only important from emission perspective but also from socio-economic perspective too. It was found that the income of a house is closely related to the selction of fuel. Thus LPG and other cleaner fuels are more popular in urban and sub-urban areas than the rural areas using wood mostly leaving fuel wood and biomass as fuel options for rural areas [6]. But with the introduction of biogas and bottled LPG supply to the rural areas, the idea of 'easy to develop' or 'homemade' clean cooking system has become imperative in recent times.

While modeling an ejector pump burner small scale firing system, most important things are to develop a proper air entrainment system for mixing purpose that will provide not only a suitable temperature but also a clean burning to reduce environmental emissions, as well as to optimize the geometry of tube and injector, and studying different fuel injection conditions. The fuel jet drags the surrounding air through the entrainment and subsequently gets mixed in the mixing tube and this primary air entrainment is controlled by momentum transfer from fuel jet to surrounding air before the combustion takes place. Thus amount of fuel supplied as well as flow rate are extremely crucial to study the air entrainment model. For different equivalence ratio (ϕ), which is related to the entrainment of air (described in Equation 4.2) , in a lean premixed condition, it can cause periodic flame extinguishment and, consequently, a periodic heat addition process that drives instabilities in the system [7]. So, depending on the geometry and heating requirement, operating at a suitable equivalence ratio is important as it governs the rich or lean condition. Current researches are focused on controlling three dangerous pollutants emitted in combustion such as: CO, CO_2 and NOx . It drives towards the inclination to the leaner condition and considering the problem of flame stabilization within the idealized parameters to control noxious elements emission. Figure 1.1(a) presents the relationship of how different chemical species are varying with the change in equivalence ratio.

Proper attention should be given on flame stability in case of a premixed combustion. Premixed burners must be designed carefully to avoid blow-off and flashback phenomena as they are extremely prone to acoustically and convective coupled instability. Small change in fuel-air mixture could make a huge impact on flame dynamics and heat distribution. In practice, it's hardly possible to ensure the full mixing of air and fuel prior to combustion and thus it results a flame which is partially premixed. In some special conditions, these types of flames exhibit better stability than a fully premixed flame operating with same global stoichiometry. Thus in depth research and understanding of such flames are of paramount important while designing a firing system. Too much of fuel, or too little fuel and excessive amount of air or insufficient primary aeration can shift the proper working zone towards soot formation, lifting of flame away or propagation of flame inside the tube as depicted in Figure 1.1(b) [8]. Thus modeling of ejector pump firing system heavily depends on parametric relationship (tube and injector diameter, distance between tube and injector) as well as injection condition (flow rate of fuel).

Moreover, a proper and efficient firing system design requires accurate modeling with the help of commercially available or open source numerical tools as well as experimental techniques. The finite
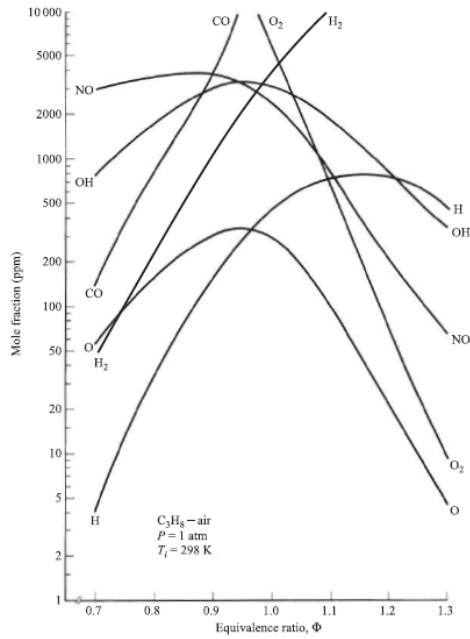
(a) Mole fraction of species vs. ϕ (b) Flame stability variation with power input
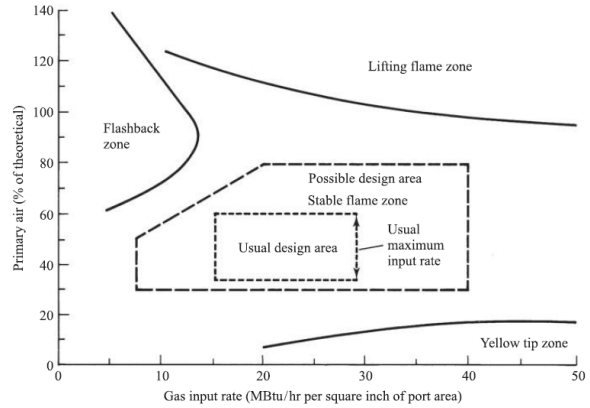
Figure 1.1: Variation in mole fraction of different chemical species during propane combustion with change in equivalence ratio (a) and flame stability region based on fuel gas input rate and primary aeration (b) [8].

element method (FEM) has been proved as a robust and reliable tool for combustion modeling which includes the complex physics of fluid dynamics, chemical kinetics, waves, diffusion and heat transfer. FEM based formulation processes a large number of discretized elements and also handles different types of element within the domain [9]. Furthermore, it also provides good results for a coarse mesh. It can easily handle complicated geometries, variable material characteristics, and different accuracy demands. To investigate any system with complex physics as well as to predict the behavior of different properties, CFD environment can guide researchers and industries while developing the real object. It also helps to understand the deviation from the experimental values. As a result, it's important to set proper guidelines in order to investigate the firing system working on ejector pump principle.

Finally, it is intended in this research work to design and provide guidelines for an easy to operate, cheap, low emission and flexible cooking system that can work with different types of fuel. As mentioned earlier, without oxidizer no combustion could take place, thus primary focus should be given on air entrainment system as well as influence of different parameters on the burner. A simple remixed combustion model will be developed and validated by using non-intrusive diagnostic techniques.

1.2 State of the Art

Most of the research have been carried out so far include both numerical and experimental investigations. Depending on the fuel types, firing conditions, burner geometry and applications, the research outcomes vary significantly. The main aims of research regarding most of the burner systems are to improve thermal performance as well as to reduce pollutant emissions by developing and modifying geometry as well as

the combustion environment.
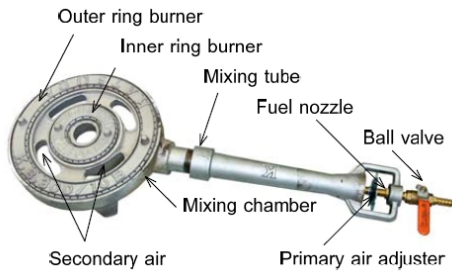
(a) General scheme of a self aspiration burner
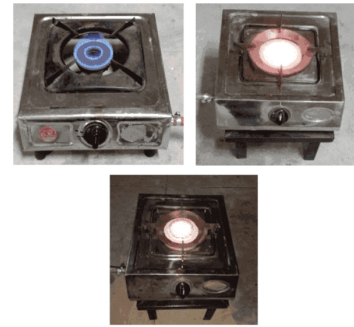
(b) Simple self aspirating cooking stove

Figure 1.2: Scheme of a self aspirated gas burner (a) reproduced from [10] and photograph of domestic cooking stove (b) [11].
.

Some interesting facts were observed while performing the research. Primary air entrainment increased significantly with the increase of momentum rate of fuel gas in the early stage but later became stable due to the constraints regarding size of mixing tube and burner port. Notable variation was observed also while performing cold and hot test and PIV (Particle Image Velocimetry) technique showed that hot test provided 22% lower primary air entrainment than the cold test due to preheating effect generated by combustion. It was also recommended to take preheating effect into consideration while designing the mixing tube chamber [12].

Incomplete combustion can lead to higher level of CO emission. For this reason, accurate prediction of primary air entrainment is of paramount importance while designing ejector pump burner. Pritchard et al. [13] proposed a simplified formulation in order to calculate the primary air entrainment based on energy and momentum conservation principles for the mixing procedure inside a circular shaped tube. The results clearly showed that level of primary air entrained is a function of type of fuel gas, fuel gas flow rate, mixing tube geometry, injector geometry and the burner.

Singh et al. [14] developed a finite element model (FEM) in order to predict the amount of primary air entrainment. The results were to be compared with the theoretical ones from [13]. It was observed that the numerical results were near to the theoretical ones, as primary air entrainment becomes higher for a higher density of fuel gas. The aspect ratio (ratio of tube and injector diameters) and density ratio were found to be the key factors influencing entrainment and mixing. They are also responsible for causing instability in jet as well as recirculation in the mixing tube. It was also observed that Reynolds number has a negligible effect on entrainment ratio. Later an experimental study [15] was performed for the same purpose and then compared again with the results from [13]. The result showed that measured amount of primary air entrained was higher for a higher ratio of burner port to injector orifice diameter. In the experiment [15], entrainment ratio increases to a maximum value as the jet location is taken away from the tube inlet. For the configurations investigated, enhancement up to 30% has been noticed in the entrainment ratio with shift in jet location. For a smaller tube diameter and jet located at the inlet of the tube, the circular jet entrains more air than non-circular jets. When the length of tube increases or

shifted jet locations, the non-circular jets entrain more of ambient fluid. Among the various non-circular geometries taken for investigation, the jet having the cross section of an isosceles triangle causes maximum entrainment.

A 1D (one-dimensional) model was developed for investigating a low NOx emission ejector pump burner [16]. The model was calibrated and validated with an experimental setup for different geometries and firing conditions. It predicted a model for air entrainment in a fully premixed, atmospheric, ejector pump burner for domestic cooking and heating applications. It took into account the buoyancy and combustion effects on air entrainment mechanism. Later, the excess air ratio (λ) which is the inverse of equivalence ratio (ϕ) was predicted as function of fuel type, geometry of burner, firing rate and ambient conditions. The combustion products (NOx, CO_2, CO) were also analyzed. Limitation of the model is that it's accurate upto ($\lambda_{model}/ \lambda^*$) around 0.85. It was also observed that increasing the diameter of mixing tube and injector also increases the primary burner aeration (λ). Additionally, increasing the height of the mixing tube as well as rounded inlet instead of straight one also facilitate primary burner aeration. But opposite behavior was established between firing rate and primary burner aeration.

Computational fluid dynamics (CFD) modeling can give important insights regarding steady state flow, combustion and heat transfer characteristics in a burner [17]. After design modifications based on results from three dimensional (3D) CFD modeling, the proposed burner showed a 2.5% of increased thermal efficiency for liquefied petroleum gas (LPG) fired burner and 10% for pipeline natural gas (PNG) fired burner. The CFD model didn't simulate the exact experimental setup and that's why improvement in percentage efficiency was compared between model predictions and experiments rather than taking absolute values into account.

One of the key things while performing different investigations regarding development of premixed burners where air entrainment plays a very important role, is to lower the emission of NOx. Controlling the operating parameters e.g. velocity of fuel and air injections along with fuel temperature and the temperature of pre-heated air control the emission of NOx significantly [18]. Moreover, reducing temperature of the charge, there is an increase in excess air ratio, which allows a considerable decrease in NOx emission and the concentration is kept within international standards [19]. Also, advantage of premixed combustion has been found also in literature as it notably decreases the NOx emission as no fuel NOx and prompt NOx are produced. Because these elements are responsible for the rise in thermal NOx. Increasing the mixing effect in mixing chamber, NOx and CO emissions were found to be less than the regular burners existing in the market [20, 21].

Fuel jet performance through a nozzle and entraining air for combustion in a gas burner has also been studied which is based on momentum conservation for 1D flows. Design charts were generated where the entrained air to fuel flow is related to the area ratio of the two streams at the plane of the nozzle. The ratio is a function containing parameters such as inlet and outlet resistance, density of fluid and Mach number of nozzle. It was observed that if the property variations are neglected, it introduces only a little percentage of error which are likely to be considered for this type of combustion cases. Mass entrainment of an injector for Reynolds number ranging from 2000 to 12000, feeding a mixing tube of 7.5 diameters can be anticipated to within 10% for a different ranges of Mach number and fluid densities in the nozzle.

In case there is failure to treat the property variations accurately in conservation equations, gives an error of only 3% [22]. Figure 1.3(a) represents the developed ejector pump model in the referenced work.
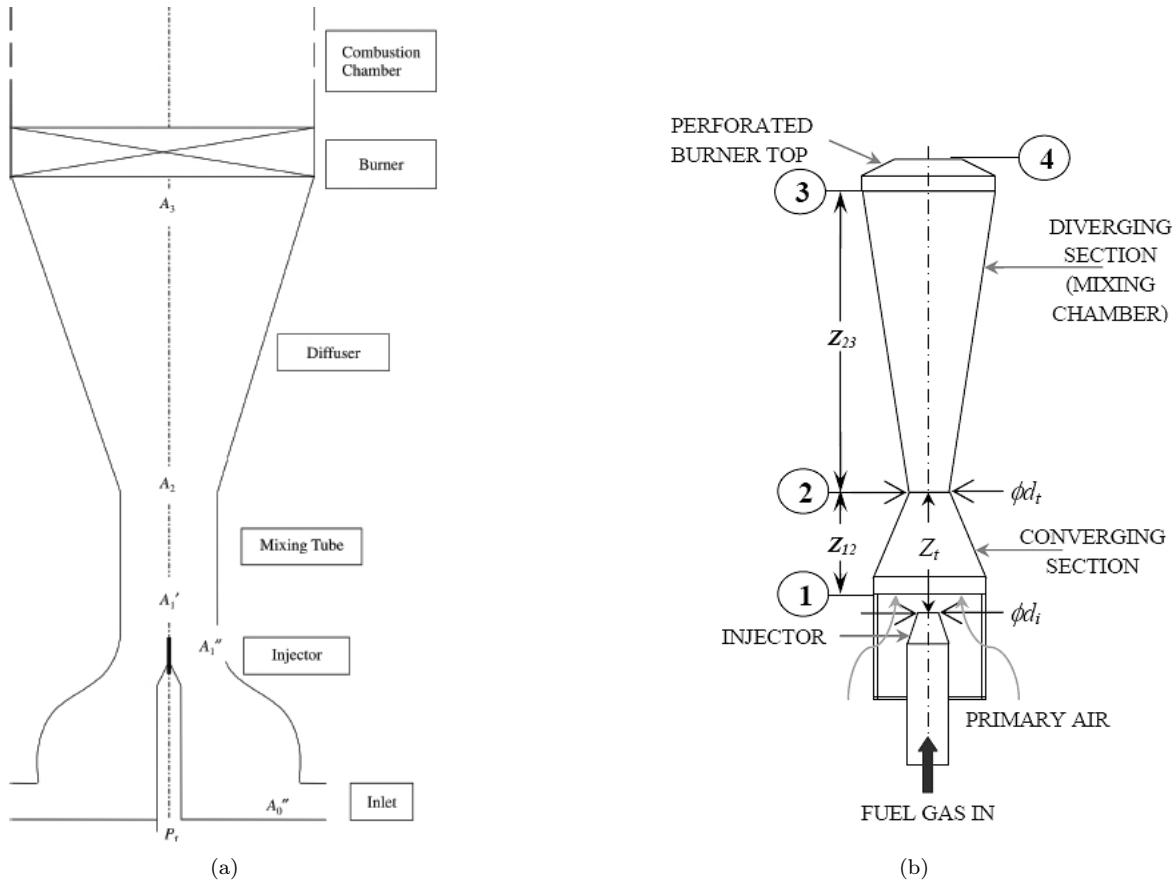
Figure 1.3: Different ejector systems (a) for gas burner [22] (b) for naturally aspirated burner [23]
.

Sutar et al. [23] developed a mathematical model for fluid flow and heat transfer through the burner depicted in Figure 1.3(b) in order to predict the primary aeration. Model predictions were used to make comparison of buoyancy effect while designing the burner. The developed method gives (48 to 73%) more primary aeration than the model developed by Jones [24] which didn't take into account of buoyancy effect (18 to 52 %). But without buoyancy effect, the former burner showed 0 to 32% primary aeration comparing to the developed one with buoyancy effect. With the new design, thermal efficiency of the burner increases from 53 % to 88 % and emissions of CO were found to be within acceptable limits.

While designing an ejector pump firing system, the air-air modeling is easy and helpful for the initial approach to understand the physics and pumping power of the system. CFD tool can be very convenient regarding this method [25]. $k - \epsilon$ model gives an overall deviation below 10% when compared to the experimental data of a home made air injector whereas less agreement was found for $k - \omega$ model. It was also interesting to see that air entrainment rate which is considered as a global performance parameter isn't sufficient enough for carrying out an accurate and trustworthy assessment for wide range of operating conditions. It's also believed that good and accurate results are closely attributed on setting up a testing facility with boundary conditions and geometric parameters as close as possible to CFD. It has been observed that for ejector modeling, turbulent modeling isn't a fully answered question for its operation

and the predictions regarding flow physics. Even though for on-design conditions, the $k - \epsilon$ provided best results but the $k - \omega$ model should also be investigated along with SST model for more detailed study during off-design predictions. Interestingly it was observed that for same entrainment rate prediction throughout a wide range of conditions, very different local flow structures could be obtained.

In an ejection refrigeration system, the overall performance mainly depends on the ejector itself. Therefore, an investigation on the characteristics and an efficient design of the ejector has been performed in CFD environment to improve the system [26]. The two parameters indicating ejector performance are entrainment ratio and critical back pressure. Previous experimental works prior to this numerical investigation were quite limited in the testing conditions. There CFD technique allows to investigate ejector performance in various conditions to suggest the best possible solution. It is found that a higher entrainment ratio can be achieved when the nozzle exit position is moved further from the ejector inlet (towards negative direction). Doing so, the effective area in the ejector throat gets bigger and therefore, entrainment ratio is higher. It should be noted that there's only one optimum position. If the nozzle exit is moved far, the momentum of the primary gas will be lower and cause a lower entrainment ratio. Thus, CFD tool has been proved in this case to decide the most suitable nozzle exit position in the actual system under specific operating conditions. Research concluded that the operating conditions and ejector shape directly affect the ejector performance. In reality, one ejctor doesn't perform well at all conditions and experiment and thus CFD technique is very useful for investigating different types of ejectors.

CFD tools can also be helpful to optimize the firing system by taking into consideration the changes geometrical parameters injectors, such as diameter and exit position. Zhao et al. [27] observed that the natural gas-air mixing process inside the mixing chamber shows that methane concentration uniformity increases with the increase of distance from injector exit. It was found that injector outlet position at -3.0 mm enhances the overall performance of premixed cylindrical burner, and also when the injector diameter is not less than 1.6 mm. Emission characteristics of NOx and CO were examined experimentally. Load factor's ((actual heat load/design heat load) x 100%) influence on NOx and CO was observed but it gradually disappeared with air coefficient isn't below 1.4. Also, with an injector position of -3.00 mm, diameter not less than 1.6 mm and also when air coefficient isn't less than 1.4, NOx and CO emissions are less than 20 ppm (parts per million) and 50 ppm respectively.

Large Eddy Simulation (LES) tool was used to investigate the flame dynamics of a swirl stabilized lean premixed prevaporized burner [28]. Flashback and blow-off regimes were identified both experimentally and numerically. Numerical approach was able to give the correct reproduction of flashback and blow-off regimes and vital role of axial reticulation zone and swirl for flashback was also shown. Potentiality of using LES to study the transient and turbulent phenomena of flames has been explored. a simple flame index is used in order to determine the local flame regime. For some regions, having an equivalence ratio above 0.8 exhibited the presence of diffusion flames and unburnt gases. Non-premixed flames dominated the flashback regime whereas compact regimes exhibit only premixed flames for normal operating condition.

As the current thesis also intends to evaluate the equivalence ratio (ϕ) of ejector pump burner both by chemiluminescence spectroscopy as well as numerical method, a detailed literature review has been made

regarding this. Emission of OH^*, CH^* and C_2^* can be used to detect the heat release and determine the equivalence ratio. Strong dependence among these parameters have been reported by Hardalupas and Orain [29]. Lean and rich combustion regions are investigated based on the intensity of OH^*/CH^* and C_2^*/CH^*. Uncertainties upto 5% and 20% have been reported while using different radical ratios for lean and rich conditions and later a correlation was developed.

1.3 Objectives

The main objective of this thesis is to develop an air entrainment model for an ejector pump system that is usually used in the household kitchen stoves. The fuel-air equivalence ratio (ϕ) will be estimated for different setup and fuel injection conditions by CFD as well as non-intrusive diagnostic techniques (PIV and spectroscopy).

CFD modeling in *COMSOL Multiphysics* will be used at first with grid independence test to choose the proper mesh settings for carrying out the simulation along with the selection of suitable physics as well as boundary conditions. Near wall treatment, mesh refinement and corner refinement are going to be done for higher level of accuracy. At first, cold test with only air as working fluid will be performed in order to test the pumping system and its efficiency by plotting different characteristics curves establishing relationship with air entrainment ratio, injection velocity and injector as well as tube geometry. An optimized limit is going to be determined for the distance between the tube and injector and the diameter of the tube based on the behavior of air entrainment ratio. Furthermore, the amount of air entrained for different configurations will be calculated from the CFD package which will later be validated from PIV.

Following the previous approach, isothermal cases for different conditions will be investigated by PIV where air will serve as the fuel in stead of C_3H_8. These isothermal cases (without flame) from PIV will be compared with the cases from isothermal models developed in the CFD environment by deactivating the non-isothermal physics. Amount of air entrainment will also be compared for both real and ideal injector geometries for validation with PIV.

Later, combustion modeling is going to be done by taking the chemical kinetics into account as well different other physics such as: turbulent flow, transport of concentrated species, heat transfer in fluids, reacting flow and non-isothermal flow. One step propane combustion reaction will be used. The flame temperature, amount of air entrained, entrainment ratio, equivalence ratio and the distribution of mole fraction from different products of combustion (H_2O, CO_2) will be investigated. Two step reaction mechanism will be also shown for few cases just for understanding CO emission and it's behavior with equivalence ratio. In order to validate the results experimentally, same configurations will be used in PIV non-isothermal case (with flame). The results will be compared later.

Finally, results from chemiluminescence spectroscopy are to be used to estimate equivalence ratio. For these specific conditions, CFD model results will be used for comparison. Chemiluminescence spectroscopy test will be performed on different geometries but for comparison, only one tube will be chosen and the result will be compared with the ones obtained from CFD analysis.

It's worth mentioning again that the main focus of this thesis will remain on the investigation of the

air entrainment for ejector pump system to setup proper guidelines for designing purpose of simple, cheap and convenient cooking stove which is usable in rural and urban areas and that can use different types of fuels, notably biogas. The numerical model uses one step combustion mechanism of propane and it doesn't predict the emission of different harmful particles for the environment even though controlling and investigating emission is very important. For understanding the general mechanism of two step reaction as well as emission of pollutant , two combustion modeling cases with two step reaction will be presented with discussion regarding pollutant and mass fraction distribution. As the first and most crucial step for designing ejector pump firing system involves the prediction of air entrainment, thorough investigation regarding this physics will be covered in this work. Propane has been chosen as the primary fuel but based on the findings, guidelines can be set for designing burners using other fuels.

1.4   Thesis Outline

The thesis is divided into five chapters where the first one provides information regarding the problem, fundamentals, scopes, contemporary and the past works done in this field. A detailed literature review has been done in this chapter in order to compare and discover the differences and similarities to other research works with the current one. Chapter 2 contains copious information related to the governing equations that are involved in the physics of CFD environment. Geometry development, grid generation and setting up proper physics have been discussed in this chapter. In the following chapter, the experimental setup information with schematic diagram and real lab photographs have been included along with the information regarding different equipment. The basic working principle, specifications, schematic diagram and photograph of the lab experimental setup of two non-intrusive diagnostic techniques namely, Chemiluminescence Spectroscopy and Particle Image Velocimetry have been provided in Chapter 3. Later, Chapter 4 contains the detail analysis with experimentally and numerically obtained data by establishing relationship among different parameters. Relationship of different geometric parameters with entrainment ratio has been investigated for better understanding of their influence on air entrainment model. Different characterizing parameters from a simple one step premixed combustion model, such as temperature, distribution of mass fractions have been provided with suitable images derived from the CFD environment. Also, a two step mechanicsm model has been presented to discuss CO emission and its relation with equivalence ratio. In some cases, while discussing, previous research papers were also used to support the findings as well as the approach for investigating the system. Finally, Chapter 5 summarized the whole research and the main conclusions briefly. Further recommendations and scopes for the future work are also enumerated.

Chapter 2

Numerical Modeling Approach in CFD Environment

CFD is a virtual prototyping tool that guides to build precision flow models by solving different transport equations. The combustion flow features can be analyzed in detail with CFD. Temperature, mixing of different species, flow velocity, concentration and flame stability, and concentration of combustion species can be computed for different types of model geometries with high level of accuracy [30].

The chemical and physical phenomena of the reacting flow may be simulated by solving a generalized set of conservation equations numerically which includes the equation for conservation of mass, momentum (Navier Stokes equations) and energy. Additional equations are required for modeling turbulence and combustion. The fundamental approach for numerical simulation of the governing equations is the finite element or finite difference approximations. Four steps methods have been employed in this application [31] involving

- The problem domain has a simple mesh.

- Values of the numerical solution are labeled at the intersections or nodes of the mesh.

- A finite element or finite difference approximation to the differential equations is formulated in each node resulting in a system of finite element or finite different algebraic equations.

- The system of equations which approximates the problem, is solved to generate a numerical solution.

In order to experimentally validate the simulation results, non-intrusive diagnostic techniques such as chemiluminescence spectroscopy and PIV have been proved as robust tools for determining the equivalence ratio (ϕ) and imaging the flow field, respectively. Quantitative measurement of the optical emission from excited elements of chemical species is investigated by the first technique whereas PIV provides instantaneous velocity vector measurements in a cross-section of a flow by using laser pulses and high resolution camera to visualize and quantify desired flow field.

2.1 Modeling Framework for Turbulent Combustion

Different forms can be used to express the governing equations for turbulent combustion flows but they are usually represented as transport equations featuring overall continuity, momentum and additional scalars which can be used to spatially and temporally- resolve the thermodynamic state of the mixture. Initial and final boundary conditions and other physics such as: reaction, molecular diffusion, equation of state are required to prepare the system of equations. As a result, in addition to density, transport equations for combustion are finally extended considering momentum and composition (e.g. mole and mass fractions, species concentration or density) as well as a scalar measure of energy (e.g. enthalpy, temperature or internal energy). The following instantaneous governing equations presented are for a reacting flow, which are in non-conservative and compressible form for the mass density, momentum, species mass fractions and internal energy [32].

Continuity:

$$\frac{\partial \rho}{\partial t} + \nabla \cdot \rho \mathbf{u} = 0 \tag{2.1}$$

Momentum:

$$\rho \frac{D\mathbf{u}}{Dt} = \rho \frac{\partial \mathbf{u}}{\partial t} + \rho(\mathbf{u} \cdot \nabla)\mathbf{u} = -\nabla p + \nabla \cdot \tau + \rho \sum_{k=1}^{N} Y_k \mathbf{f}_k \tag{2.2}$$

Species continuity (k=1,...,N):

$$\rho \frac{DY_k}{Dt} = \rho \frac{\partial Y_k}{\partial t} + \rho \mathbf{u} \cdot \nabla Y_k = \nabla \cdot (-\rho \mathbf{V}_k Y_k) + \omega_k \tag{2.3}$$

Energy:

$$\rho \frac{De}{Dt} = \rho \frac{\partial e}{\partial t} + \rho \mathbf{u} \cdot \nabla e = -\nabla \cdot \mathbf{q} - p\nabla \cdot \mathbf{u} + \tau : \nabla \mathbf{u} + \rho \sum_{k=1}^{N} Y_k \mathbf{f}_k \cdot \mathbf{V}_k \tag{2.4}$$

In the above equations, ρ, u and p respectively represent the mass density, the velocity vector and pressure; f_k is the body force associated with the kth species per unit mass; τ is the viscous stress tensor; V_k is the diffusive velocity of the kth species, where the velocity of the kth species may be expressed as the sum of the mass-weighted velocity and the diffusive velocity, u+V_k; Y_k stands for the mass fraction of the species k; ω_k is the kth species production rate; mixture internal energy is denoted by e, which may be expressed as:

$$e = \sum_{k=1}^{N} h_k Y_k - p/\rho \tag{2.5}$$

q is the heat flux, which represents heat conduction, radiation, and transport through species gradients as well as Soret effect, and h_k is the kth species total enthalpy.

From Equations 2.2, the term for pressure and viscous stress tensor τ can be formulated as:

$$\tau = \mu \left[(\nabla \mathbf{u}) + (\nabla \mathbf{u})^T \right] + \left(\frac{2}{3}\mu - \kappa \right) (\nabla \cdot \mathbf{u})\mathbf{I} \tag{2.6}$$

where μ is the dynamic viscosity; κ is the bulk viscosity; and I is the identity matrix.

Also, the diffusive mass flux $\rho Y_k \mathbf{V}_k$ from Equation 2.3 represents the transport of species along with their transport with the bulk flow, $\mathbf{u}$. Diffusive mass transport are associated with mass or species concentration gradients, known as the Fickian diffusion, and temperature gradients known as Dufour effect, and pressure gradient. A hierarchy of models concerning diffusive mass flux can be considered and the first one is based on adopting a Fick's law model using mixture averaged transport coefficients. The diffusion velocities $\mathbf{V}_k$ can be determined using the Hirschfelder-Curtiss approximation:

$$X_k \mathbf{V}_k = -D_k^m \nabla X_k \tag{2.7}$$

where D_k^m is the mixture-averaged mass diffusion coefficient for species k. The mixture averaged mass diffusion coefficient is derived usually by using mixture weighting rules and multi component diffusion coefficients and it can be expressed as:

$$D_k^m = \frac{K}{\rho c_p \mathrm{Le}_k} \tag{2.8}$$

In the above equation, c_p is the mixture specific heat, K and Le_k respectively present mixture thermal conductivity and Lewis number of kth species.

2.2 The k-ω Turbulence Model

Two-equation models are very popular for describing turbulent flows and are currently used by all commercial and open source CFD packages. Here, along with the mean-flow Navier–Stokes equations, two more transport equations for two turbulence properties are solved. The first one is turbulence kinetic energy (k) and the second one can be any other from a variety that includes: dissipation rate of turbulence kinetic energy (ϵ), the specific rate of dissipation (ω)(the dissipation of turbulent kinetic energy (k) into internal thermal energy), the length scale (l), the product of k and l, the time scale τ, the product of k and τ [33].

The k-ω model is a successful model which has been used widely for several reasons. It also exhibits superiority over the k-ϵ model. For example, it achieves higher accuracy for boundary layers with adverse pressure gradient and can be easily incorporated in the viscous sub layer in the absence of any additional damping functions. The initial model was proposed by Kolmogorov in 1942 [34]. Further improvement of the model was done by Spalding [35]. According to the latest development by Wilcox [36], the model can be formulated as follows that includes the equations governing the turbulent kinetic energy and specific dissipation rate.

Eddy viscosity:

$$\mu_T = \rho k/\omega \tag{2.9}$$

Turbulent kinetic energy

$$\frac{\partial}{\partial t}(\rho k) + \frac{\partial}{\partial x_j}(\rho u_j k) \quad = \rho \tau_{ij}\frac{\partial u_i}{\partial x_j} - \beta * \rho k \omega + \frac{\partial}{\partial x_j}\left[\left(\mu + \sigma^*\frac{\rho k}{\omega}\right)\frac{\partial k}{\partial x_j}\right] \tag{2.10}$$

Specific dissipation rate

$$\frac{\partial}{\partial t}(\rho \omega) + \frac{\partial}{\partial x_j}(\rho u_j \omega) = \alpha\frac{\omega}{k}\rho \tau_{ij}\frac{\partial u_i}{\partial x_j} - \beta\rho\omega^2 \quad + \sigma_d\frac{\rho}{\omega}\frac{\partial k}{\partial x_j}\frac{\partial \omega}{\partial x_j} + \frac{\partial}{\partial x_j}\left[\left(\mu + \sigma\frac{\rho k}{\omega}\right)\frac{\partial \omega}{\partial x_j}\right] \tag{2.11}$$

Closure coefficients

$$\alpha = 13/25, \quad \beta = 3/40, \quad \beta^* = 9/100, \quad \sigma = 1/2, \quad \sigma^* = 3/5, \quad \text{Pr} = 8/9 \tag{2.12}$$

$$\sigma_d = \begin{cases} 0, & \frac{\partial k}{\partial x_j}\frac{\partial \omega}{\partial x_j} \leq 0 \\ \sigma_{do}, & \frac{\partial k}{\partial x_j}\frac{\partial \omega}{\partial x_j} > 0 \end{cases}, \quad \sigma_{do} = \frac{1}{8} \tag{2.13}$$

2.3 Chemical Kinetics Modeling

The net source of chemical species i due to reaction R_i is computed as the sum of the reaction sources over the N_R reactions that the species participate in and the model has been built according to Poinsot and Veynante [37].

$$R_i = M_{w,i}\sum_{r=1}^{N_R}\hat{R}_{i,r} \tag{2.14}$$

M_w, i is the molecular weight of species i

$\hat{R}_{i,r}$ is the molar rate of creation destruction of species i in reaction r

The rth reaction rate can be written as:

$$\sum_{i=1}^{N}\nu'_{i,r}\mathcal{M}_i \overset{k_{f,r}}{\rightleftharpoons} \sum_{i=1}^{N}\nu''_{i,r}\mathcal{M}_i \tag{2.15}$$

Where,

M_i symbol donating species i

N number of chemical species in the system

$\nu'_{i,r}$ stoichiometric coefficient for reactant i in reaction r

$\nu''_{i,r}$ stoichiometric coefficient for product i in reaction r

The molar reaction rate of creation/destruction of species i in reaction r is given by:

$$\hat{R}_{i,r} = \Gamma\left(\nu''_{i,r} - \nu'_{i,r}\right)\left(k_{f,r}\prod_{j=1}^{N_r}[C_{j,r}]^{\eta'_{j,r}} - k_{b,r}\prod_{j=1}^{N_r}[C_{j,r}]^{\eta''_{j,r}}\right) \tag{2.16}$$

N_r number of chemical species in reaction r

$C_{(j,r)}$ molar concentration of each reactant and product species j in reaction r $[kgmol/m^3]$

$\eta'_{i,r}$ forward rate exponent for each reactant and product species j in reaction r

$\eta''_{i,r}$ backward rate exponent for each reactant and product species j in reaction r

Γ represents the effects of third bodies on the reaction rate:

$$\Gamma = \sum_{j}^{N_r} \gamma_{j,r} C_j \tag{2.17}$$

Here, $\gamma_{j,r}$ is the third body efficiency of the jth species in the rth reaction.

In Eddy Dissipation Model (EDM), reaction rates are assumed to be controlled by the turbulence and thus computationally expensive Arrhenius chemical kinetic calculations are avoided. The model is computationally cheap but in order to apply to solve realistic cases, only one or two step heat-release mechanisms should be used. It was introduced by Spalding [38] for premixed combustion modeling. EDM postulates that the reaction will occur only if the breakup of the turbulent structures reaches the finest turbulent scales. In other words,the basic concept behind EDM is reaction must be faster than the turbulent mixing of substrates thus making the Damkohler number (Da) much greater than 1 and it's valid for the fast burning fuels. The assumption is taken for a very fast chemistry and turbulent mixing time is the dominant time scale. This can be applied for both turbulent premixed and non-premixed combustion. In EDM, The mass source due to reaction is calculated from,

$$\dot{\omega}_{kj} = v'_{kj} M_k \rho A \frac{\epsilon}{k} \min \left(\frac{Y_i}{v'_{ij} M_i} \right) \tag{2.18}$$

$$\dot{\omega}_{kj} = v'_{kj} M_k \rho A B \frac{\epsilon}{k} \sum_{p=1}^{N_p} Y_p / \sum_{i=1}^{N} v''_{ij} M_i \tag{2.19}$$

Model constants A and B are respectively 4 and 0.5

2.4 Model Development in Commercial CFD Package

For the computational approach, designing the 2D axisymmetric model, grid generation and executing the required physics for modeling have been carried out by licensed commercial *COMSOL Multiphysics* version 5.4 CFD environment. The burner studied in this model includes mainly two components which are the mixing tube with considerable wall thickness and the injector. Two different injector geometries, namely *ideal* and *real* have been considered to investigate the performance of the ejector pump system. By using ideal geometry, it was also intended to investigate the performance of the system and understand its behavior in order to develop a homemade, easy to operate cooking system. Appropriate boundary conditions are applied for respective physics settings while developing the CFD code. The following subsections include detail information regarding computer aided design of the system, mesh generation and selection of proper physics and solver for carrying out the numerical simulation.

2.4.1   Geometry Design

Figure 2.1(a) is the schematic 2D diagram of the firing system comprised of the injector and the mixing tube. The original tube has a length of 10.1 cm with an external diameter of 1.5 cm as well as 0.25 cm of thickness. The material is stainless steel with a straight inlet and outlet shape. The symbols L and D respectively represent the height of the tube and the external diameter whereas d and l denote the diameter of the injector and height respectively. The mixing tube has a small wall thickness t and the distance between tube and injector has been denoted by Δ.

The injector is 3 cm long and in this investigation, two different fuel injectors of different diameters (1 mm and 0.76 mm) have been considered. The test bench has clamps and base metal plate for supporting the system and the injector is connected with computer controlled gas feeding system. All the dimensions in the modeling environment's design modeler have been parameterized in order to facilitate the change in geometry based on tube diameter, injector diameter and distance between injector and mixing tube. The parameterized drawing in CFD environment is placed in Appendix B.

Figure 2.1(b) represents the different mass flow rates involved during the process with direction. $\dot{m}_f$ is the amount of fuel injected through the injector. Due to the dragging effect, the ambient air is sucked through the bottom of the mixing tube and the amount of air entrained is denoted by $\dot{m}_{ae}$. Both masses are mixed inside the tube and exit with a mass flow rate of $\dot{m}_m$. There are little amount of secondary air entrainment also at the top of the tube where the mixture exits and the flame is developed.

(a) Dimensionalized sketch of the setup   (b) Flow direction of working fluids
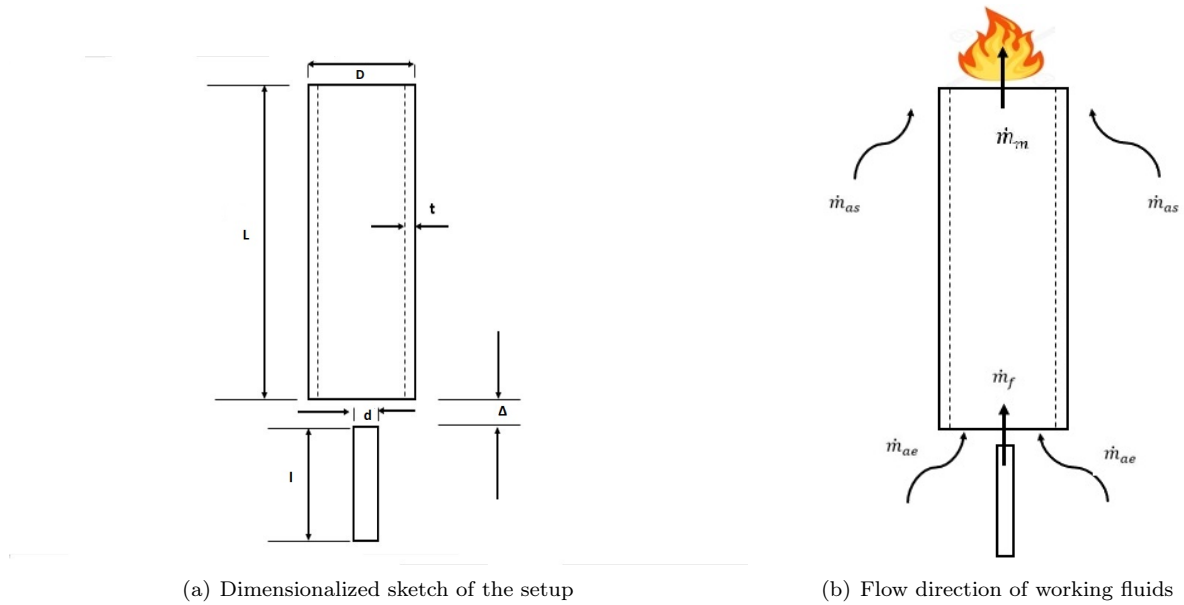
Figure 2.1: 2D sketch of the tube and injector with various dimensions and entrainment.

For the initial test runs, the distance between the tube and injector was kept 1 cm. Later the parameterized dimensions were modified in order to investigate the effects of distance Δ on the pumping system and combustion characteristics. Additionally, the diameter of the tube has been modified also by increasing and decreasing from the original diameter while keeping the length same. The purpose was to observe the effect of tube diameter on air entrainment ratio. Furthermore, the injector shape was also modified later in order to investigate the aforementioned phenomena. For combustion model, the ideal

injector geometry has been used whereas to investigate the effect of geometry modification of injector, a comparison concerning pumping efficiency which includes entrainment ratio has been performed between them. A computer aided design shows the detail geometry of the system with the actual dimensions in Figure 2.2 and Figure 2.3 depicts the 2D axisymmetric design in the modeling environment. The detailed geometry of the injectors are provided in Figure 4.2. The real injector outlet is converged whereas the ideal injector diameter remains same throughout the length. The axes z and r define the axis coordinate system in the design environment. Throughout the work, axis z will stand for the vertical coordinate system and axis r will represent horizontal coordinate system that is the radial distance from the center line.
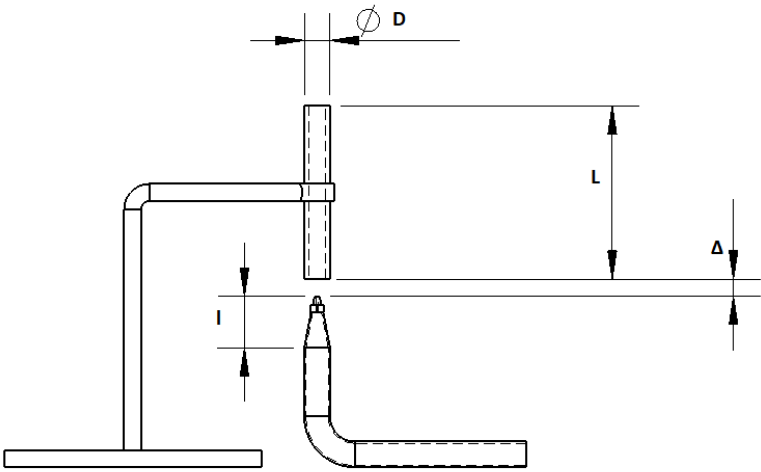
Figure 2.2: Computer Aided Design of the setup and injector.
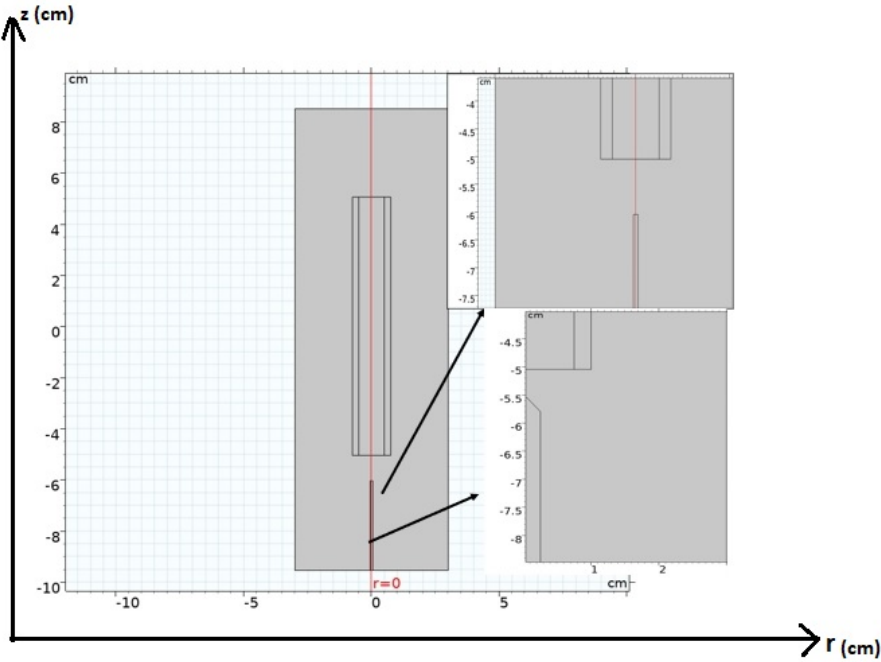
Figure 2.3: 2D axisymmetric drawing in COMSOL design environment with ideal and real geometry.

16

2.4.2 Grid Generation

One of the most important tasks in finite element analysis is to develop a suitable and accurate mesh in order to reduce error and make the solution much closer to the expected value. In this experiment, generating a refined and appropriate grid was of paramount importance as it took into account high speed gas injection velocity, air entrainment due to injection, turbulent mixing, wall thickness and flame development at the top of the tube and secondary air entrainment. *COMSOL's* mesh generating environment provides the user to properly set the parameters including *maximum element size minimum element size*, *maximum element growth rate*, *curvature factor* and *resolution of narrow region* in order to build a finer mesh. Among these, *maximum element size* limits the allowed element size whereas *minimum element size* specifies the minimum allowed size of an element. To determine the maximum rate at which the element size can grow from a region with small elements to a region with larger elements is set by *maximum element growth rate* and finally *curvature factor* sets the ratio between the boundary element size and the curvature radius in order to determine the size of boundary elements compared to the curvature of the geometric boundary. Throughout all the simulations performed to investigate this system, the element sizes were calibrated for fluid dynamics interface and the element size parameters were set by using CFD environment's default predefined "extra fine" meshing feature which includes the following grid information presented in Table 2.1 following a grid independence test discussed in section 2.4.3.

Element size parameters	Values
Maximum element size	0.039 cm
Minimum element size	4.5E-4 cm
Maximum element growth rate	1.08
Curvature factor	0.25
Resolution of narrow regions	1

Table 2.1: Grid size information for "extra fine" mesh setting

For structuring the grids inside the injector and the mixing tube, mapped face meshing has been used as it refers only to structured meshing of four sided, 2D regions and when the face is approximately rectangular. Because of its simplicity of implementation and capability of producing high quality of mesh, it has been a popular choice in commercial mesh generators [39]. The basis of mapping is transfinite interpolation. The settings for the size and distribution nodes used by a mapped node calculate the density of the logical meshes. For generating the mesh in the external domain, triangular elements have been used with the same governing element size parameters. *Smooth across removed control entities* feature ensures to smooth the transition in element size across removed control entities. For further accuracy, refinement feature has been applied to refine the mesh by splitting into more elements. For the near wall treatment, the wall of tube and injector were treated with dense element distribution to resolve the thin boundary layer along the no-slip boundaries. The developed mesh can be described as a hybrid mesh as boundary layer, mixing tube and injector are discretized with structured cells whereas the remaining part uses unstructured also known as triangular cells. While treating the near wall, boundary layer stretching factor and thickness adjustment factor have been kept at 1.2. Several grid settings with

different element numbers have been used and based on the grid independence test which is discussed in result section, the proper setting is selected.

(a) Grid generated for upper half

(b) Grid generated for lower half
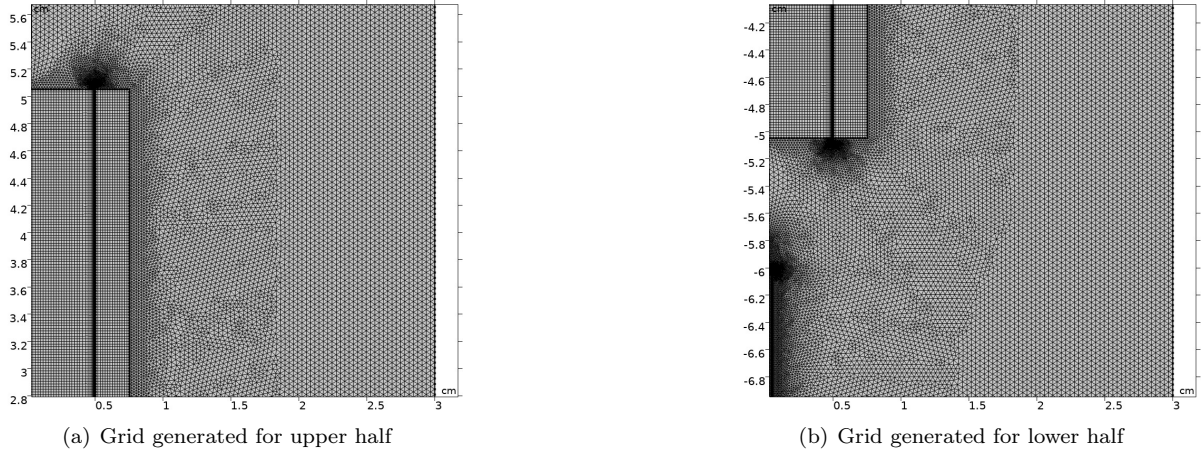
Figure 2.4: Final mesh generation for the model (a) upper half, (b) lower half.

(a) Near wall treatment for injector

(b) Near wall treatment for tube
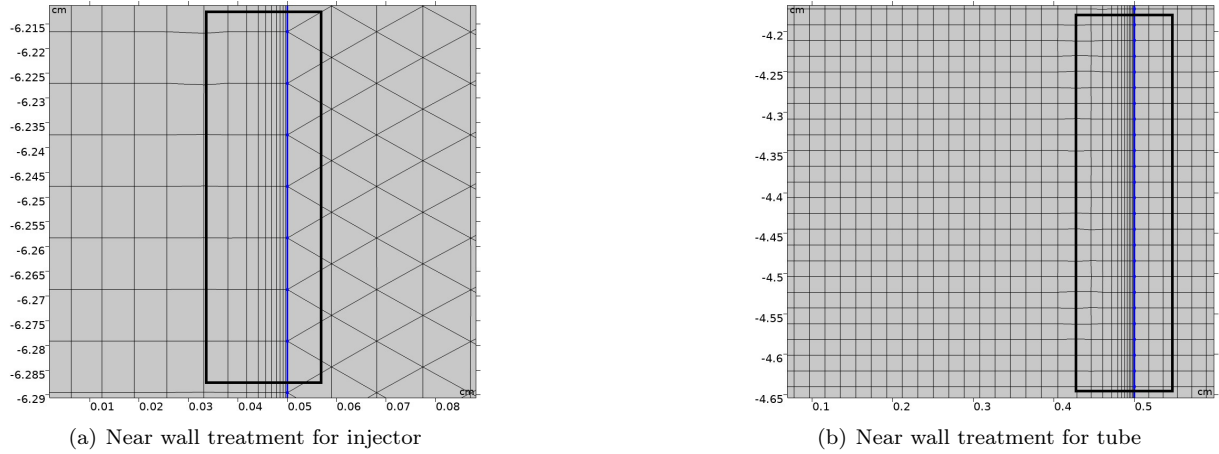
Figure 2.5: Wall treatment with boundary layers for tube and injector (a) injector wall, (b) tube wall.

In Figure 2.4, the mesh generated for the computational model has been represented in two parts (upper and lower). Figure 2.4(a) depicts the meshing for the tube exit to the surrounding and Figure 2.4(b) is the view of meshing done for fuel injection and the entrance of fuel and entrained air through the bottom of the tube. From both figures it can be observed that special care has been taken for the zones with higher velocity gradient (mainly for air entrainment and fuel injection). The total number of elements has been set around 189k after the grid independence test. Four different types of elements, namely: triangles, quad, edge and vertex constitute the whole mesh structure. Figure 2.5 shows the close-up view of the tube and injector walls where no-slip condition has been applied and the near wall regions have been divided into more sub-layers (7 and 8 respectively for injector and tube) for taking into account the variations of different fluid properties during the flow. Total mesh area was around 37 cm^2 and the average element quality was found to be 0.94.

Figure 2.6 shows the distribution of grid quality in terms of skewness factor throughout the computational domain. Quality of the element never reached below 0.3 and only few elements have been

observed with such scale near the regions where a rapid and sudden change in fluid properties, such as velocity, are taking place. The mesh resolution and element quality are important aspects to consider when validating a model. Low mesh resolution can lead to inaccurate results. A low mesh element quality which measures the regularity of the mesh elements' shapes can lead to inverted mesh elements and to high condition numbers for the Jacobians, which in turn, can be causing problem in convergence issues. The mesh element quality is a dimensionless quantity between 0 and 1, where 1 represents a perfectly regular element, in the chosen quality measure, and 0 represents a degenerated element. Skewness is the default quality measure which is a measure of the equiangular skew and defined as:

$$Skewness = 1 - \max\left(\frac{\theta - \theta_e}{180 - \theta_e}, \frac{\theta_e - \theta}{\theta_e}\right) \tag{2.20}$$

Where θ is the angle over a vertex (2D) or edge (3D) in the element, θ_e is the angle of the corresponding edge or vertex in an ideal element, and the minimum is taken over all vertices (2D) or edges (3D) of the element. This quality measurement is based on the equiangular skew which penalizes elements having large or small angles comparing to the angles of an ideal element.

(a) Element quality(tube outlet)   (b) Element quality(tube entrance)   (c) Element quality(injector outlet)
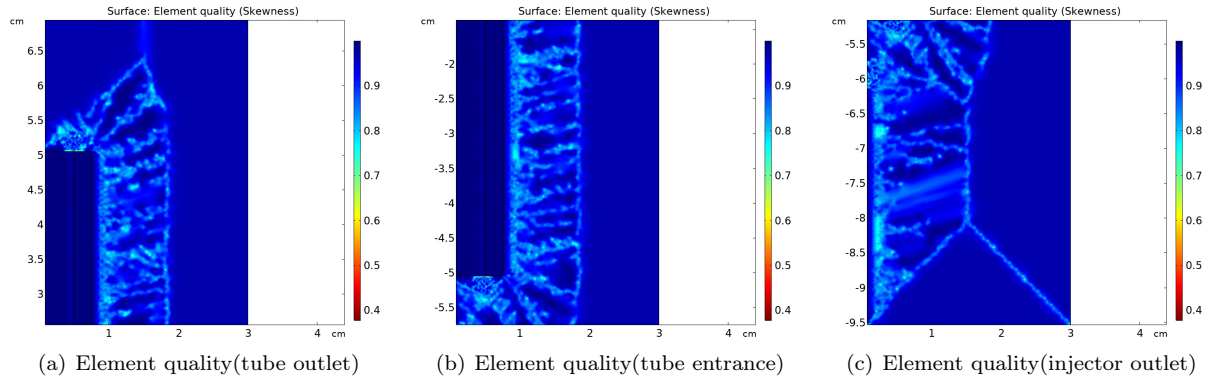
Figure 2.6: Quality of grid in terms of skewness factor.

2.4.3   Grid independence test

As discussed in Figure 2.1 and Figure 2.3, the geometry of the system is quite simple but due to air entrainment and air injection, it is important to take care of the mesh properly in order to obtain better accuracy in results by using the computer's available resources. As a result, before running all the simulation cases, it is important to set an approximate mesh settings that includes number of cells, refinement near the wall boundary as well as other important parameters. That's why a grid independence test has been performed to select the proper setting where there will any significant deviation in the output results.

Figure 2.7 shows the variation of entrainment ratio (defined in Equation 4.1) with different grid settings. Significant variations have been observed while the cell numbers varied in between 5000 to 50000. Later with more refinement, results were also found to be changing and near 189000 elements, they exhibited steady behavior with very little change in the output results. Later, for further observation, the grid number was increased to almost 0.4 million but only 0.2% change was noticed. So, considering
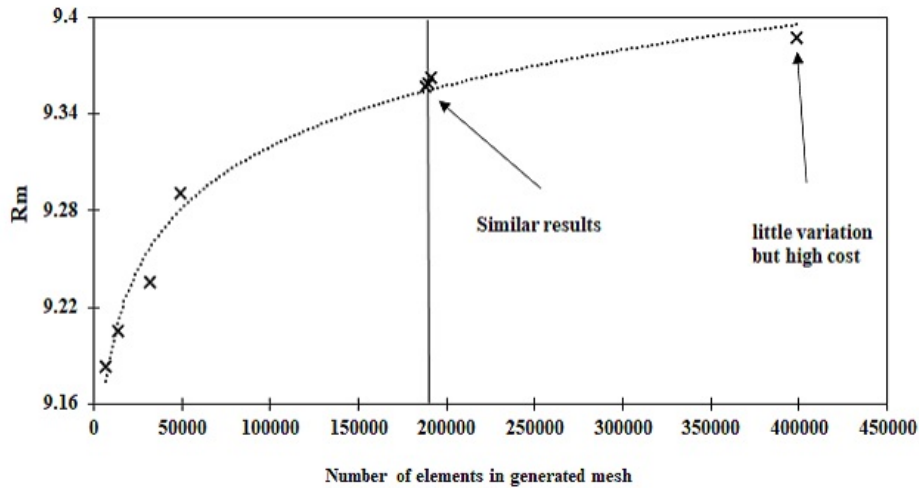
Figure 2.7: Grid independence test.

the computational cost, it was concluded to keep the grid settings corresponding to 189000 cells. After that, the parameters mentioned in Table 2.1 were selected and they were kept almost same throughout all the simulations, although they varied a little depending on the increase and decrease of tube and injector diameter. The number of cells were increased for the combustion model as the external domain height was increased for better visualization of the flame. But nonetheless, the impact of this change on entrainment ratio was very little. While optimizing a premixed cylindrical burner [27], similar test was also carried out before executing the simulations.

2.4.4   Selection of suitable physics, boundary conditions and solver

After developing the 2D geometry and setting up the appropriate grid, suitable physics needed to be selected in order to carry out the computational study. In this method, the flow has been considered as turbulent as well as the mixing process in the tube. Due to the presence and reaction of chemical species and considering both isothermal and non-isothermal condition, the features namely: *Turbulent Flow k-ω*, *Transport of Concentrated Species*, *Heat Transfer in Fluids*, *Reacting Flow* and *Non-isothermal Flow*. For each physics, it's extremely important to choose the exact boundary conditions and other necessary governing features and parameters.

The first physics that must be selected is the *Turbulent Flow k-ω* which is used for simulating single-phase flows at high Reynolds numbers. The physics interface is suitable for weakly compressible flows, incompressible flows and compressible flows at low Mach numbers (less than 0.3). The equations solved by the Turbulent Flow, k-ω interface are the Reynolds-averaged Navier-Stokes (RANS) equations momentum conservation and the continuity equation for mass conservation. Turbulence effects are modeled using the Wilcox revised two-equation k-ω model with realizability constraints. The k-ω model is a so called low-Reynolds number model, which means that it can resolve the flow all the way down to the wall. It's important to define the mixture dynamic viscosity in this physics' interface. For the wall, no slip is the default boundary condition to model solid walls. In a no slip wall, the fluid velocity relative to the wall

velocity is zero. For a stationary wall that means that u = 0. The injector entrance has been chosen as the inlet as a fully developed flow where the average velocity is set from experimentally used different volume flow rate in Standard Liters per Minute (SLPM). For a given flow rate in SLPM, which is later converted to kg/s, the velocity of injection is calculated from,

$$V = \frac{\dot{m_f}}{\rho A} \tag{2.21}$$

Where, V is velocity in m/s, A is the injection nozzle area in m^2, ρ is density of fuel in kg/m^3 and $\dot{m}$ is mass flow rate in kg/s.

The outlet is selected as pressure outlet with a value equals to zero at the physics interface level, defining it as relative pressure. The "Suppress backflow" feature adjusts the outlet pressure in order to prevent fluid from entering the domain through the boundary. For the discretiztion, P1+P1 has been used which stands for first order elements for velocity and first order elements for pressure. Linear elements are computationally cheaper than higher order elements and produce less spurious oscillations. As a result, it improves the numerical robustness for solution. This is the default element order for the laminar flow and turbulent flow for single phase interfaces and the discretization of fluids in the multiphase flow interfaces.

The Transport of Concentrated Species physics interface is used to investigate liquid and gaseous mixtures where the species concentrations have the same order of magnitude and none of them can be identified as a solvent. Here, properties of the mixture depend on the composition and the molecular as well as ionic interactions between all species. This interface includes models for multi-component diffusion in which, diffusive driving force of each species depends on the mixture temperature, composition and pressure. In this experiment, one step stoichiometric propane combustion equation has been considered and for diffusion model, the Fick's law model is used when the diffusion is assumed Fickian, meaning no multi-component diffusivities are available. In other terms, the molecular diffusion is not the dominating transport mechanism. Two additional models will be presented also by considering two step propane combustion equation by setting proper initial values in the physics environment. In order to develop the model, boundary conditions have to be defined with extreme precautions. Two inflows have been considered, one for propane injection in terms of mole fraction and another for the surrounding air in terms of mass fractions. To define the reaction mechanism, stoichiometric coefficients have been used from the general combustion equations. A suitable value for forward and reverse rate constant is set for the reaction. Eddy dissipation turbulence reaction model identifies that turbulent flow will be accounted for in the reaction mass sources.

For modeling the heat transfer in fluids by conduction, convection and radiation, the *Heat Transfer in Fluids* physics has been chosen which allows to define the flow and direction of heat as well as heat source (ignition source) and other fluid properties, such as thermal conductivity, gas constant and specific heat capacity at constant pressure. The enthalpy of formation for the stoichiometric propane combustion equation serves as the heat source for the reaction. Four interpolation functions have been formulated in order to calculate the heat capacity at constant pressure for C_3H_8, O_2, H_2O and CO_2. Using the relation between mass fraction, molar mass and specific heat, the average C_p of the mixture is defined. For inflow

boundary condition, it applies in inflow of heat coming from a virtual domain, that was excluded from the model for the simplification of analysis, known as upstream conditions. Applied at inlets, the inflow condition accounts for temperature and pressure from upstream phenomena. An initial guess temperature of 298K has been taken for the initial value. The *Heat Transfer in Fluids* solves the following equation.

$$\rho C_p \left(\frac{\partial T}{\partial t} + \mathbf{u} \cdot \nabla T \right) + \nabla \cdot (\mathbf{q} + \mathbf{q}_\mathrm{r}) = \alpha_p T \left(\frac{\partial p}{\partial t} + \mathbf{u} \cdot \nabla p \right) + \tau \cdot \nabla \mathbf{u} + Q \tag{2.22}$$

In Equation 2.22, the dependent variables are the temperature T and pressure p. The different quantities used here are C_p, ρ , T and u respectively representing specific heat at constant pressure, density of fluid, temperature and velocity vector. Also q is the heat flux by conduction (unit: W/m^2, $\mathbf{q}_\mathrm{r}$ is the heat flux by radiation (unit:W/m^2) and α_p is the thermal expansion coefficient (unit: 1/K). And Q contains heat sources other than viscous dissipation (unit: W/m^3).

The *Multiphysics* module contains any physics features that are likely to be used as multiphysics coupling for a particular set of physics interfaces added to the model builder. Different approaches are attributed to the use of the multiphysics coupling feature. It is either predefined while adding a specific physics interface or it is automatically added when the software recognizes logical coupling in the model design. To solve this computation, two different modules, *Reacting Flow* and *Nonisothermal Flow* have been used.

The *Reacting Flow* multiphysics coupling is used to simulate mass transport and reactions in a gas or liquid mixture where the fluid flow can be dependent on the mixture composition. When added, the density in the single phase flow interface is automatically synchronized to the one defined by the Transport of Concentrated Species interface. Conversely, the velocity field used by the latter interface is synchronized to the one computed in the former interface. The coupled interfaces allow the coupling of physics from turbulent flow and transport of concentrated species. Kays-Crawford has been selected as the mas transport turbulence model.

For investigating multiphysics coupling to simulate fluid flows where the fluid properties depend on temperature, the *Nonisothermal Flow* physics has been used. As a result, it synchronizes the features from the *Heat Transfer in Fluids* and *Turbulent Flow k-ω* fluid interfaces when a turbulent flow regime is defined. After setting up all the necessary boundary conditions corresponding to respective physics, the model has been prepared for executing the computation by running the solver. The stationary study steps are used when field variables do not change over time, such as in stationary problems and also to find the solution to linear and nonlinear stationary problems (also called static or steady-state problems). All three physics interfaces and the two multiphysics couplings are executed by the solver including the generated mesh. Under the stationary solver, segregated solver is used in order to compute unknown variables, which are velocity, pressure, turbulence variables (turbulent kinetic energy and the specific rate of dissipation), mass fraction of the reactants and products of combustion and temperature. The Finite Volume Solution Method can either use a segregated or a coupled solution procedure. With segregated methods an equation for a certain variable is solved for all cells, then the equation for the next variable is solved for all cells.

Chapter 3

Experimental Investigation with Spectroscopy and PIV

In this section, the instrumentation of the general experimental setup, including flow meter and fuel supply connection as well additional setup for spectroscopy and PIV will be discussed. The general schemes, laboratory photographs and basic working principle with equipment specifications will also be provided.

3.1 Experimental Setup and Instrumentation

The basic setup of the experiment is simple and requires less supporting equipment. A schematic of the general experimental setup (without spectroscopy and PIV) used in this work is presented in Figure 3.1. In order to ensure safe and proper flow of fuel to the system, the main propane intake has been taken through a computer controlled flow meter which is operated by the *Alicat* developed *Flow Vision* software. The flow meter used here has a capacity of passing 5 SLPM flow through it with $\pm 0.4\%$ accuracy. Using this general setup, blowoff and flashback limit for the particular tube and two different injectors have been determined. These limits have been used later in the experimental setup using PIV and spectroscopy. The flow rates were maintained in a suitable range within flashback and blowoff limit. The whole setup has been supported on metal base plate with proper clamping and fastening arrangement.

The working fluids properties (in STP) involved in this experiment is presented in Table 3.1.

Property	Air	Propane
ρ [kg/m^3]	1.25	1.882
μ [Pa.s]	1.81×10^{-5}	8.196×10^{-6}
Molar mass [kg/kmol]	28.96	44
LHV [MJ/kg]	-	46.4

Table 3.1: Fluid properties at STP
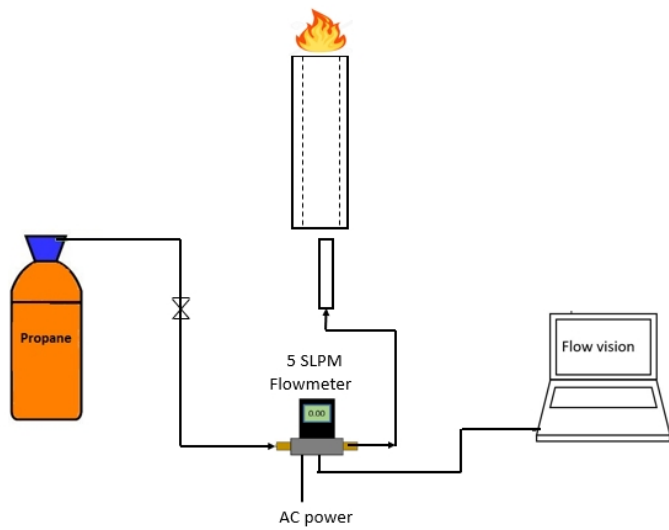
(a) General experimental schematic
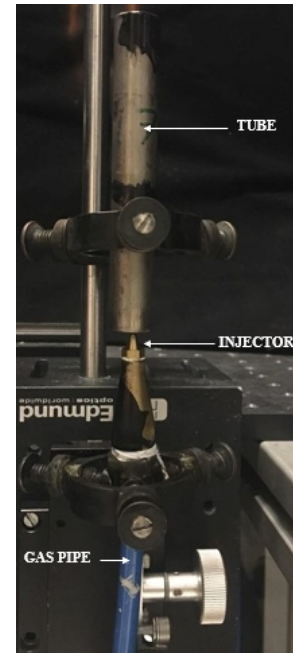
(b) Photograph of real setup

(c) Alicat flow meter

Figure 3.1: Schematic diagram and photograph of experimental setup.

3.1.1 Chemiluminescence Spectroscopy

It is very important to properly understand the chemical kinetics involved in the reaction and also to characterize it. To serve these purpose, an optical diagnostic technique known spectroscopy has been used which is based on flame chemiluminescence. It's quite straightforward, simple and non-intrusive method that offers the quantitative measurements of the optical emission from excited chemical species. For hydrocarbon flames, the radical chemiluminescence emissions of OH^*, CH^* and C_2^* can be considered as 'finger prints' for flame diagnostics [40], specially CH^* and C_2^*, corresponding to blue and green colors in visible spectrum.

The fundamental of this process is based on the spontaneous emission of electromagnetic radiation from the chemical species during the combustion process. The emitted radiation will have an intensity as well as wavelength as the excited radical is formed during reaction and goes to its ground state. The wavelength and intensity can be correlated to different flame properties uniquely based on the setup [41]. The main purpose of this diagnostic technique in this experiment is to estimate the equivalence ratio (ϕ) depending on the peak values of intensities from the emission of respective chemical radical which are OH^*, CH^* and C_2^*. The ratio of these radicals are taken subsequently. During the data acquisition, flame emission spectra from the center of a premixed propane air flames as well as the the narrow band

peaks are observed which is presented in Figure 3.2.
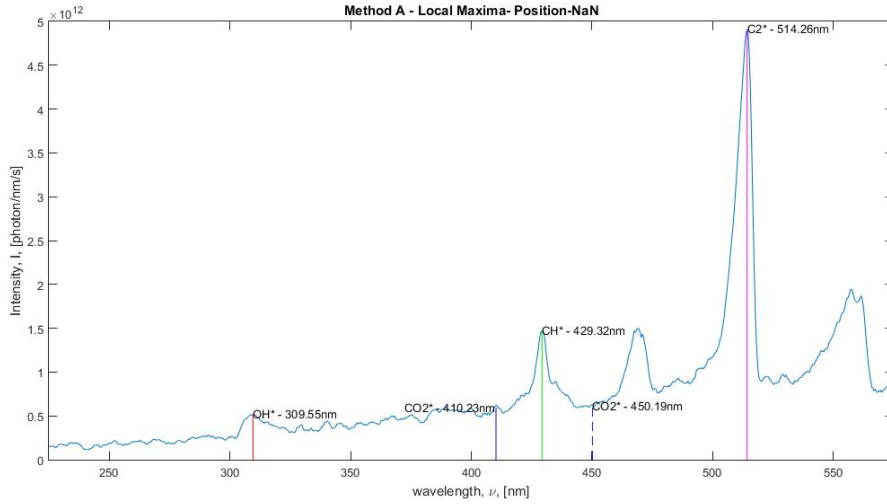
Figure 3.2: Emission spectrum during experiment.

Using three different ratios, OH^*/CH^*, C_2^*/CH^* and C_2^*/OH^*, it has been found that a correlation of equivalence ratio can be obtained [42]. It is important to pick the curve with a higher inclination and slope. Otherwise, if the curve is too horizontal or vertical, the ratio between the chemical species don't allow to predict the equivalence ratio. In a premixed flame of methane, propane and butane, intensity ratios C_2^*/CH^* were found to be proportional to equivalence ratio ϕ [43], whereas in a study conducted later, this ratio was also correlated to ϕ [44].

The experimental setup is composed of a light collector which is comprised of an optical probe with facilities to adequately adjust the distance to the flame and vertically move with flame height. An optical fiber from *Ocean Optics* with a core diameter of 400 micrometer and a solid angle of 25 degree was connected with the spectrometer which is an *Ocean Optics*, model QP400-2-SR-BX. The fibre cord is 2 m long and mostly consists of a fused silica. The collimator lens which collect the light emission in a shape of cylindrical volume by means of two adjustable diaphragm and the complete schematic is shown in Figure 3.3.

The acquired signal was received by an Ocean Optics *HR4000* spectrophotometer with a 190 to 1100 nm wavelength range and the incoming signals are processed by the *Ocean Optics* developed *SpectraSuite* software. The detail specifications of the spectrometer have been provided in Table 3.2.

Detector type	Toshiba TCD1304AP
Pixels	3648
Integration time	4ms-20s(continuous), $10\mu s$-4ms(shutter)
Power consumption	4mA, 5V DC
Signal to noise ratio	300:1
Optical resolution	0.02-8.4 nm

Table 3.2: Specifications of spectrometer.

In order to analyze the emitted radiation most accurately and with the least amount of ambient noise
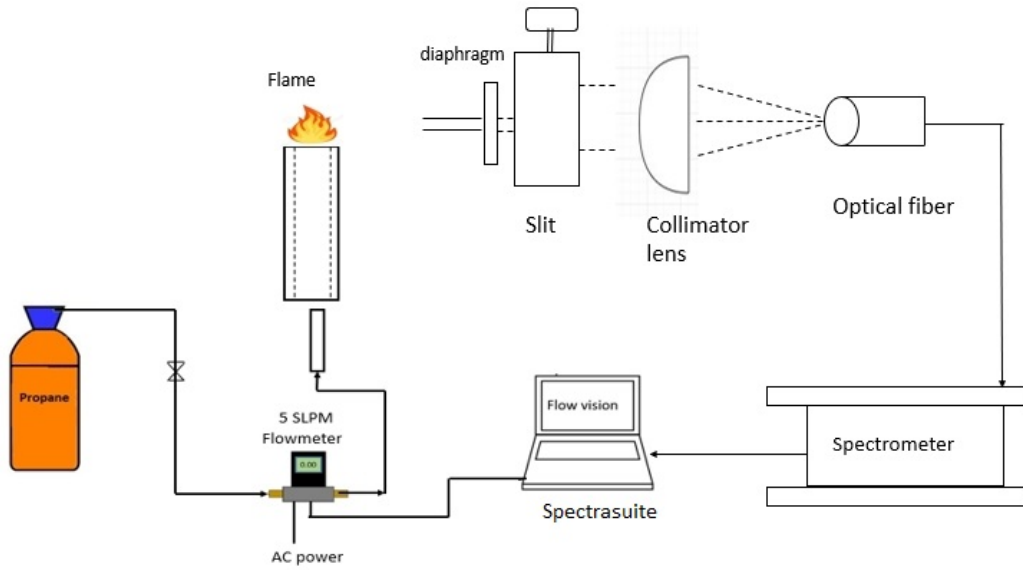
Figure 3.3: Schematic diagram of spectroscopy setup.

contamination, 100 individual spectra were taken with an integration time of 1 second each. After that, those spectra were averaged and the background test values were subtracted by using a *MATLAB* script. In order to correlate the measured values of radical intensity, captured by chemiluminescence technique, and obtaining the equivalence ratio, a calibration procedure is essential which will be discussed in the result and discussion section. The main purpose of this technique is to estimate the equivalence ratio across the flame front and also to understand the behavior of the flame under different fuel injection and setup condition. The real experimental setup photograph is given in Figure 3.4 showing all the components and measuring equipment connected during the diagnosis.
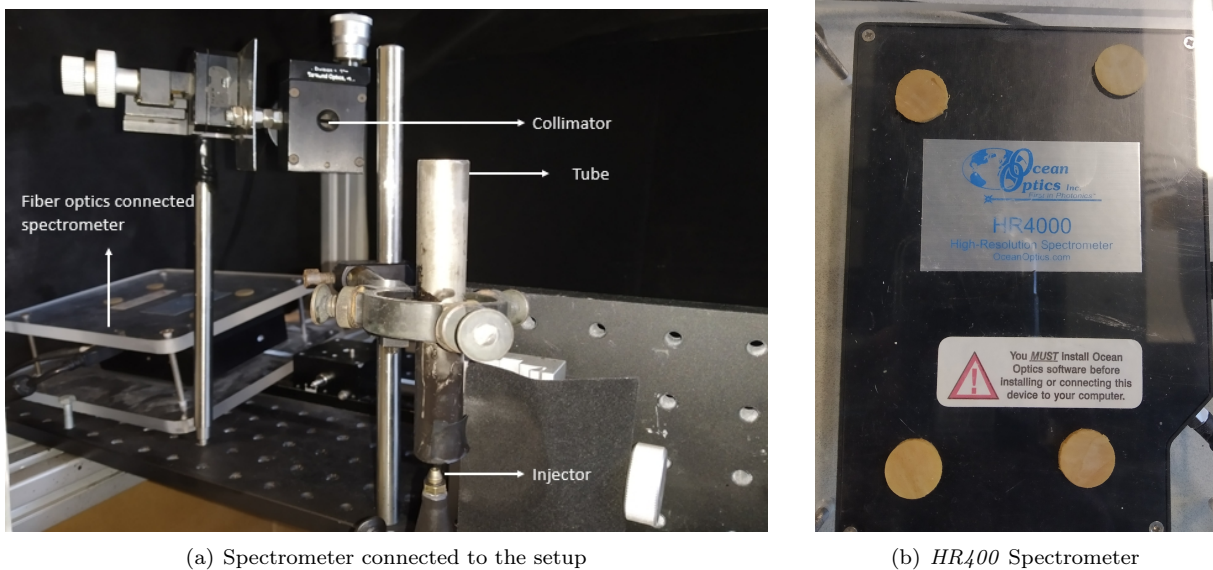
(a) Spectrometer connected to the setup

(b) *HR400* Spectrometer

Figure 3.4: Experimental setup photograph for spectroscopy

For the reference setup, the similar ejector pump system with a tube diameter of (external) 2cm and

a length of 8cm has been used along with the injector d1. The flame chemiluminescence subsequently analyzed for the interior blue reaction zone by avoiding the plume so that it can obtain different radical emission intensities for a wide range of equivalence ratios. Besides, a background spectrum was acquired over the same integration time taking into account for the surrounding radiation emission, and subtracted from each of the acquired spectra before making the average.
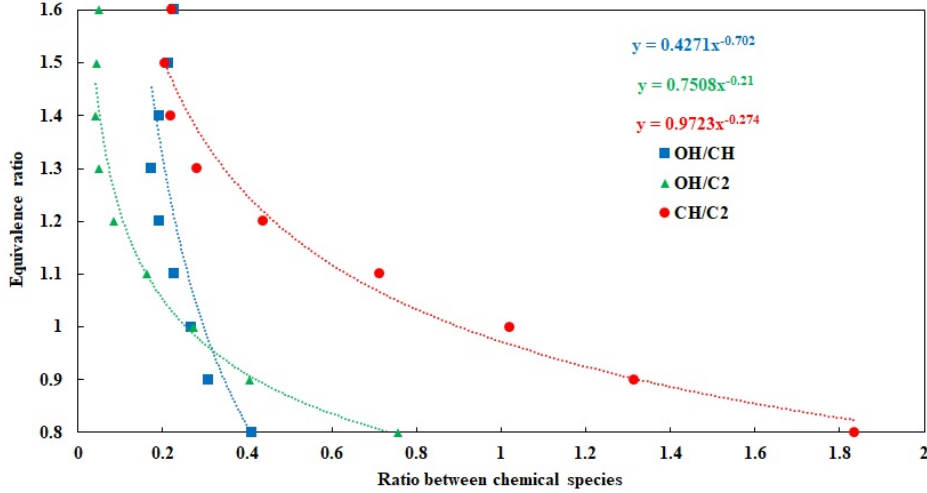
Figure 3.5: Calibration curves for equivalence ratio ranging from $\phi = 0.8$ to 1.6.

Using the data obtained from *SpectraSuite* while performing chemiluminescence spectroscopy, a *MATLAB* routing has been used to process the data and based on the ratios of the radicals OH^*, CH^* and C_2^* obtained throughout the whole equivalence ratio, calibration curves are formed which are presented in Figure 3.5. It is observed from Figure 3.5 that for a working range of equivalence ratio from 0.8 to 1.6, the ratio of different radicals exhibited different behavior. Mathematical formula can be generated establishing relationship between the equivalence ratio and the ratios between the chemical species. Thus, it is possible to use the relationship for estimating equivalence ratio for further investigation. The relationships established from the calibration curves can be expressed as:

$$\phi = 0.4271 \left(\frac{OH^*}{CH^*} \right)^{-0.702} \tag{3.1}$$

$$\phi = 0.750 \left(\frac{OH^*}{C_2^*} \right)^{-0.21} \tag{3.2}$$

$$\phi = 0.9723 \left(\frac{CH^*}{C_2^*} \right)^{-0.274} \tag{3.3}$$

The curve representing Equation 3.3 has been chosen as it has a higher inclination or slope. Otherwise, if the curve is too vertical or too horizontal, the ratios between chemical species don't allow to accurately predict the equivalence ratio. For instance, in the other curves from Equation 3.3 and 3.1, a slight difference on the chemical species ratio may change completely the equivalence ratio.

3.1.2 Particle Image Velocimetry

Particle Image Velocimetry (PIV) is a quantitative velocity measuring technique. It provides additional and significant advantages while comparing to conventional flow measurement techniques such as hot wire anemometry and doppler velocimetry because of its higher precision and non-intrusive behavior. The flow remain undisturbed by the probes thus allowing a complete velocity field measurement. Flows with seeding particles are illuminated by a light sheet of which instantaneous images are recorded by a CCD/sCMOS camera. These images are analysed from which entire flow fields are determined. The flow is undisturbed by probes allowing for a whole-field measurement of the velocity. The PIV technique can be classified into two steps, visualization and image analysis [45].

The flow is seeded with tracing particles (paraffin oil) and illuminated by a double pulsed laser in the area of investigation to produce a green light planar sheet which has a of 530 nm. The double pulsed laser is synchronized with a high speed CCD camera using a synchronizer which is connected to the primary acquisition system. The camera captures two consecutive frames of laser lighted particles seeded in the flow. After that, the 2D velocity field can be determined by making cross correlation of the two consecutive frames as well as the time interval between laser pulses and the distance traveled by the seeding particles.

The setup for PIV is mainly comprised of four major components, which are: the double pulsed laser which is produced by *Dantec Dual Power 65-15 Nd:YAG* with two laser cavities and each having a maximum laser pulse frequency of 15 Hz, along with a wavelength of 532 nm; the image acquisition system, provided by a HiSense Zyla sCMOS camera with a framerate of 40 FPS and a resolution of 2560×2160 pixels protected by 532 nm filter. Synchronization between the aforementioned components is maintained by a *BNC 575 Series Pulse Generator* which is centrally controlled by an acquisition system on a dedicated computer using *Dantec DynamicStudio* software. Dual power lasers are dual cavity flash pumped Nd:YAG (Neodymium:Yttrium aluminium garnet) lasers designed for PIV applications. The laser pulses are in the order of several nanoseconds. In most cases frequency-doubled Nd:YAG or Nd:YLF (Neodymium-doped yttrium lithium fluoride) lasers emitting green light are used.The specification for *Dantec DualPower* lasers are given in Table 3.3.

Maximum output	400 mJ
Pulse duration	4 ns
Wavelength	1064 nm, 532 nm
Laser medium	Nd:YAG
Type	Dual cavity pulse laser
Repetition rate	0-15 Hz

Table 3.3: Specifications of *DualPower* lasers.

The synchronizer serves as an external trigger for the camera and the laser. Controlled by a computer, the synchronizers can dictate the timing of each frame of the CCD/CMOS/sCMOS camera's sequence in conjunction with the filming of the laser to within 250ps .As a result, the timing between each pulse of the laser and the placement of the laser shot in reference to the camera's timing can be accurately

maintained. The synchronizer is able to acquire online measurements of the gap between the trigger pulse to the laser and the light pulse from the laser. With a resolution of 1ns to 250ps, it allows for a high accuracy laser pulse time stamping. It means a greater increase in velocity accuracy in PIV system. It is of paramount important to know this timing is critical as it's required to determine the velocity of the fluid during PIV analysis.

The particle density in the seeded flow must have a reasonable matching with the density of the main flow in order to avoid errors induce by injection velocity as well as gravitational effect as well as to maintain the main flow trajectory. Several particle characteristics must be taken into account to ensure the acquisition of valid data. The seeding particles must have good light scattering properties and as a matter of fact, they shouldn't be too small as well as non corrosive, non abrasive, non volatile, and non toxic. Due to this, the paraffin oil has been chosen as the seeding particle [46]. It should be noted that PIV does not necessarily detect the specific velocity of single seeding particle. Rather, the local velocity of a small area of the measurement plane is statistically computed based on the identification of particle patterns. Generally, 2D cross correlation schemes are applied and the two recorded images that represent the illuminated seeding particles in the flow, are divided into small interrogation windows. The pattern of an interrogation window in the first image, which is correlated with a region of equal size in the consecutive second image that is shifted pixel wise near the interrogation window of the first image. Position of the maximum correlation value in this map is the most probable displacement of the particle pattern of that specific interrogation window [47].
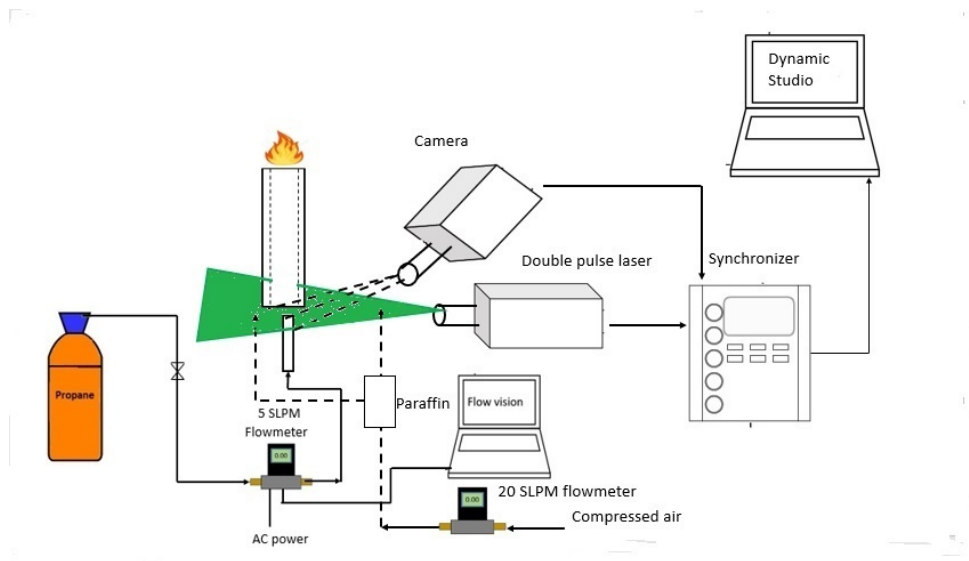
Figure 3.6: Schematic of PIV setup.

The schematic diagram of PIV setup is depicted in Figure 3.6. Compressed air has been used to force the paraffin oil from a venturi like reservoir and controlled by an *Alicat* 20 SLPM flowmeter operated by *Flow Vision* software. The green region in the diagram represents the laser sheet covering the area of interest which is the air entrainment zone and the surrounding places near the entrainment zone are seeded with the paraffin particles. As a result, the air entrained is illuminated due to the presence of the seeding particles and the instantaneous positions are captured by the high resolution camera. For

this experiment, two different nozzles have been used and cases including hot test (with flame), cold test (without flame) and air-air approach have been considered. While performing the air-air approach, the propane supply was replaced by the compressed air supply. During cold test, CO_2 has been used instead of propane as it has same molar mass and also to avoid the waste of propane gas.

After the stabilization of the surrounding with proper seeding particle density and distribution, the laser focus length has been adjusted to the camera center's view field establishing a laser sheet in the area of interest. Camera and laser sheet remained perpendicular and the tube's bottom part and injector's metal surface were painted black to avoid reflection of the laser. The procedure for post processing the raw data acquired by the PIV will be discussed in the Chapter 4. The lens of camera was protected by a *Meller Griot 352 nm filter*. In Figure 3.7, the photograph of the lab setup for PIV is illustrated.
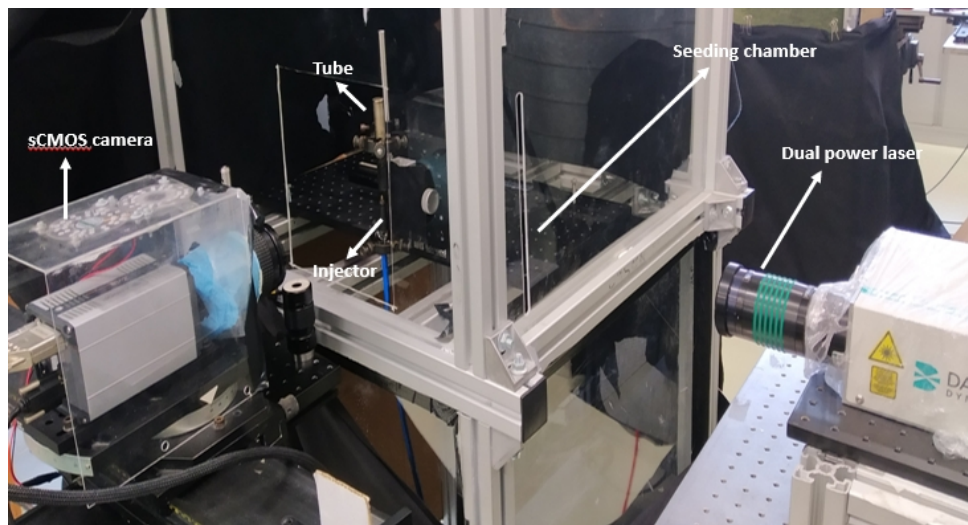
Figure 3.7: Photograph of the PIV setup.

Chapter 4

Results and Discussions

In this chapter, all the findings from CFD simulations as well as laboratory experiments will be discussed. Also, the validation of each technique (CFD, Chemiluminescence Spectroscopy and PIV) will be done and the variation of results from each other will be discussed. The chapter is divided in five sections named as: *Results from Numerical Modeling (Air-air approach)*, *Combustion Modeling in CFD Environment*, *Analysis of Results from Chemiluminescence Spectroscopy*, *Analysis of Results from PIV* and *Comparison of Equivalence Ratio from Chemiluminescence Spectroscopy and PIV*. The first subsection will analyze in detail regarding the influence of injector shapes and parametric study for different parameters influencing the system's efficiency. Later, results from combustion model developed by CFD simulations are presented to investigate the consistency in entrainment ratio behavior with the air-air case, flame temperature as well as mass fraction of different reactants and products of combustion. Additionally, cold test (without flame) results are also discussed and finally the equivalence ratio (ϕ) will be determined for different cases. One step propane combustion reaction has been chosen but two cases using two step mechanism are also presented to observe the effect trend of CO with air entrainment. Results from Chemiluminescence Spectroscopy and PIV will be discussed along with the explanation of data post processing.

4.1   Results from Numerical Modeling (Air-air approach)

This section includes results from the effects of different parameters related to tube and injector geometry on the pumping performance of the ejector pump system by using air-air approach. Thus, it will provide guidelines and set some optimum limits regarding different parameters while designing other systems. Effects of tube diameter (D), injector diameter (d), distance between tube and injector (Δ), injection condition ($\dot{m}_{fuel}$) will be investigated. Throughout the investigation, a ratio of mass flow rate exited from the tube ($\dot{m}_{out}$) and mass flow rate of the fuel injected ($\dot{m}_{fuel}$) from injector has been defined as as entrainment ratio(Rm) in order to define the performance of the system in terms of air entrainment.

$$Rm = \frac{\dot{m}_{out}}{\dot{m}_{fuel}} = \frac{\dot{m}_{\text{air entrained}} + \dot{m}_{\text{fuel}}}{\dot{m}_{\text{fuel}}} = 1 + \frac{\dot{m}_{\text{air entrained}}}{\dot{m}_{\text{fuel}}} \tag{4.1}$$

The entrainment ratio Rm can be also related to the equivalence ratio ϕ.

$$Rm = 1 + \frac{\left(\frac{\dot{m}_{\text{air entrained})}}{\dot{m}_{\text{fuel}}}\right)_{\text{Stoichiometric}}}{\phi} \qquad (4.2)$$

The modeling of the system with air-air has been performed with three different mixing tubes, two injectors, three injection condition and seven distances between tube and injector. The following table, Table 4.1 gives the specifications of the tube and injector used the air-air approach investigations.

Tube name	Length (L)	External diameter(D)	Thickness(t)
T1	10.1cm	2cm	0.25cm
T2	10.1cm	1.5cm	0.25cm
T3	10.1cm	1.2cm	0.25cm

Injector name	Diameter (d)		
d1	1mm	-	-
d2	0.76mm	-	-

Table 4.1: Specifications of the tubes and injectors used in the air-air investigation.

4.1.1 Influence of Injector Geometry and Diameter

(a) Schematic of burner configuration with ideal injector geometry

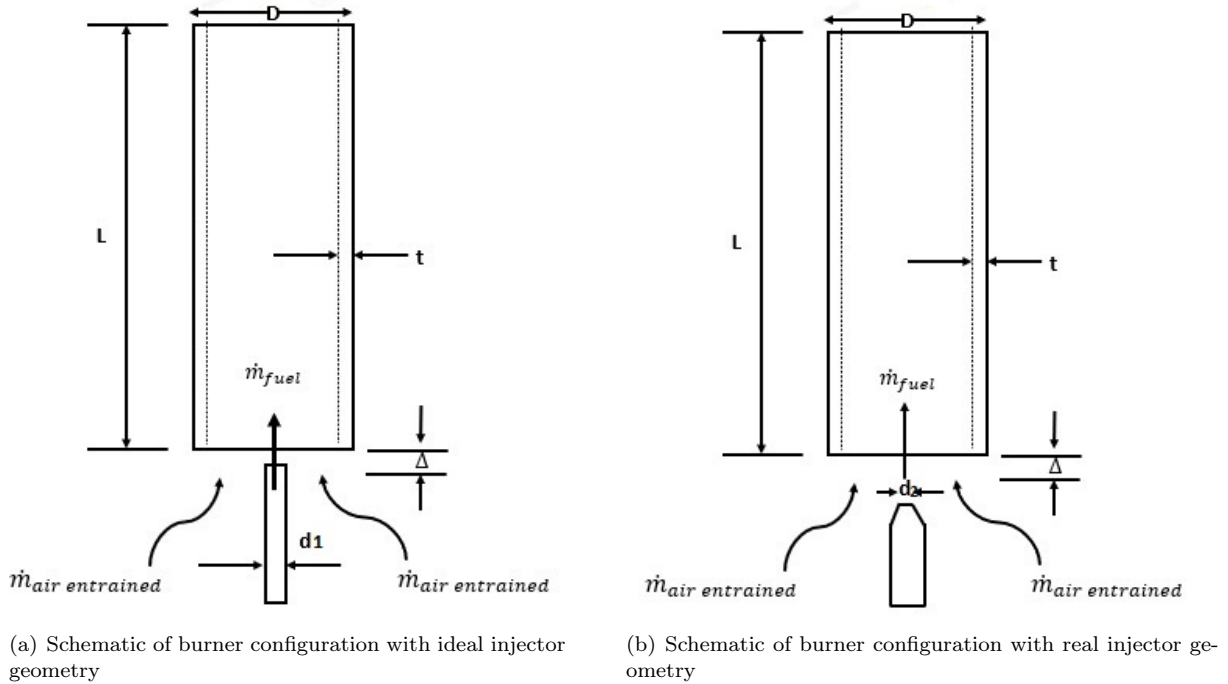(b) Schematic of burner configuration with real injector geometry

Figure 4.1: Schematic of the ejector pump system consisting of mixing tube and two burner geometries, (a)ideal and (b) real.

The geometry of the injector plays an important role on the amount of air entrained and thus affecting the equivalence ratio. Depending on the injector geometry, it is expected to observe variation in entrainment ratio. In this work, two different injector geometries have been used, namely *ideal* and *real*.

To investigate the influence of geometry change, the tests have been performed by using two different diameter injectors (1mm and 0.76mm, respectively denoted as d1 and d2) along with two different diameter mixing tube (external diameter 2 cm and 1.5cm, respectively denoted as T1 and T2) with same inlet boundary condition (volume flow rate in SLPM). Air was injected as the working fluid for these four arrangements. The length of the tubes was kept 10.1 cm in all cases. The height of the injector in both cases were 2cm and the convergence angle for real shape injector was designed at 65deg. The schematics of the setups as well as both injectors have been presented in Figure 4.1 and 4.2.
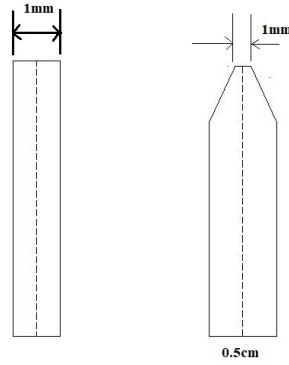
Figure 4.2: Geometry of the ideal (left) and real (right) injectors with 1 mm injection diameter.

| (a) Tube T1 | (b) Tube T2 |

Figure 4.3: Distribution of entrainment ratio for tubes T1 and T2 with d1 injector for distance Δ=0.05 to 4cm with ideal and real geometries under v_{in}=1.88 SLPM.

Figure 4.3(a) depicts the comparison between the air entrainment performance while using two different geometries for the injector. 1mm injection diameter was kept for both of them while the mixing tube external diameter was 2cm. For both geometries, with the increase in distance between injector and tube, the entrainment ratio decreases, except the position Δ =0.5cm which gives maximum value. Entrainment ratio was found to be higher in all cases for the real geometry. While the distance between tube and injector was maintained with 0.05cm to 2cm, the deviation of output results between real and ideal injector varied within 12%. But with increase in distance, deviation found to be larger and reaching 17% for 4 cm distance.

It was observed that entrainment of air decreases with the decrease in mixing tube diameter while using the d1 injector. Figure 4.3(b) represents the behavior of air entrainmment with T2 mixing tube. For distance between 0.05cm to 2cm, the deviation between two geometries were found to be little higher than the previous case but limited within 13% whereas it almost reached nearly 20% for the longer distances such as 3cm and 4cm. The previous case (T1) gives an average 1.5 to 1.6 times higher entrainment ratio for different distances. Highest value of R_m was observed at $\Delta = 0.5$cm.

While investigating with a 0.76mm injector, the entrainment ratio behaved differently. For both cases, the amount of air entrained was found to be higher than the previous investigation with 1mm injector. For the same inlet boundary condition and using the tubes T1 and T2, the characteristic graphs in Figure 4.4 describe the trend of entrainment.

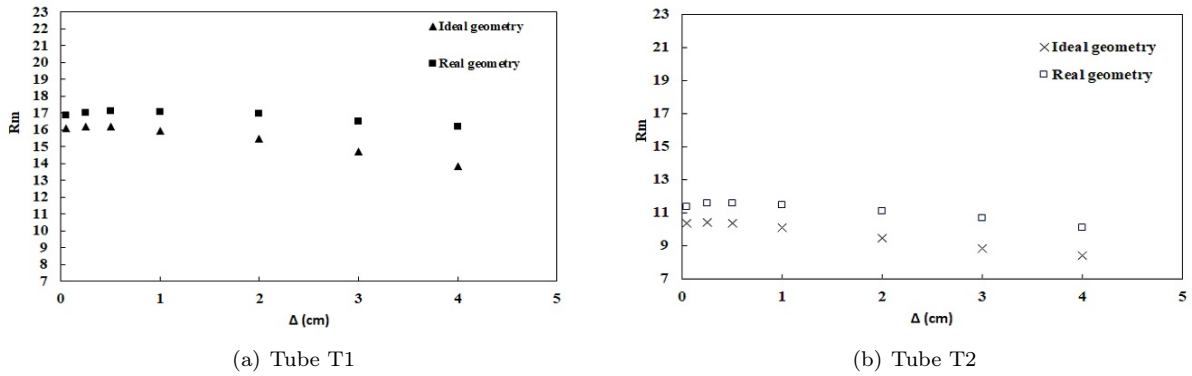(a) Tube T1 (b) Tube T2

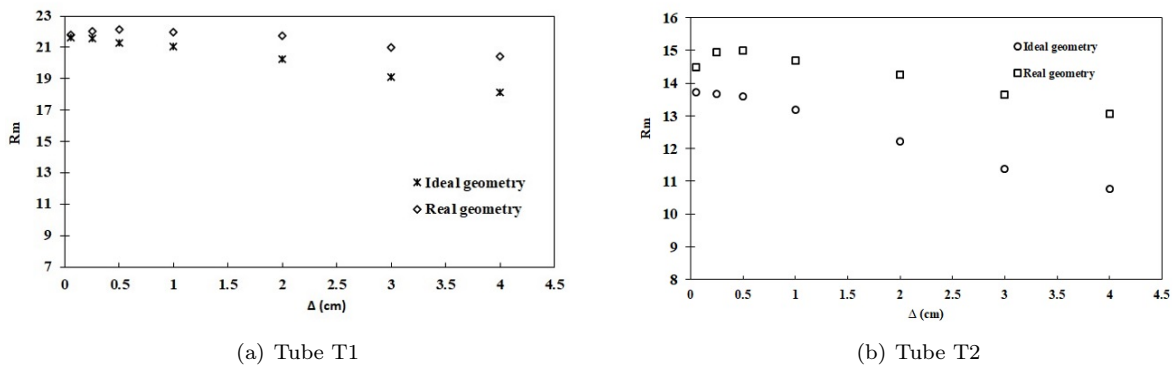Figure 4.4: Distribution of entrainment ratio for tubes T1 and T2 with d2 injector for distance $\Delta=0.05$ to 4cm with ideal and real geometries under $\dot{v}_{in}=1.88$ SLPM.
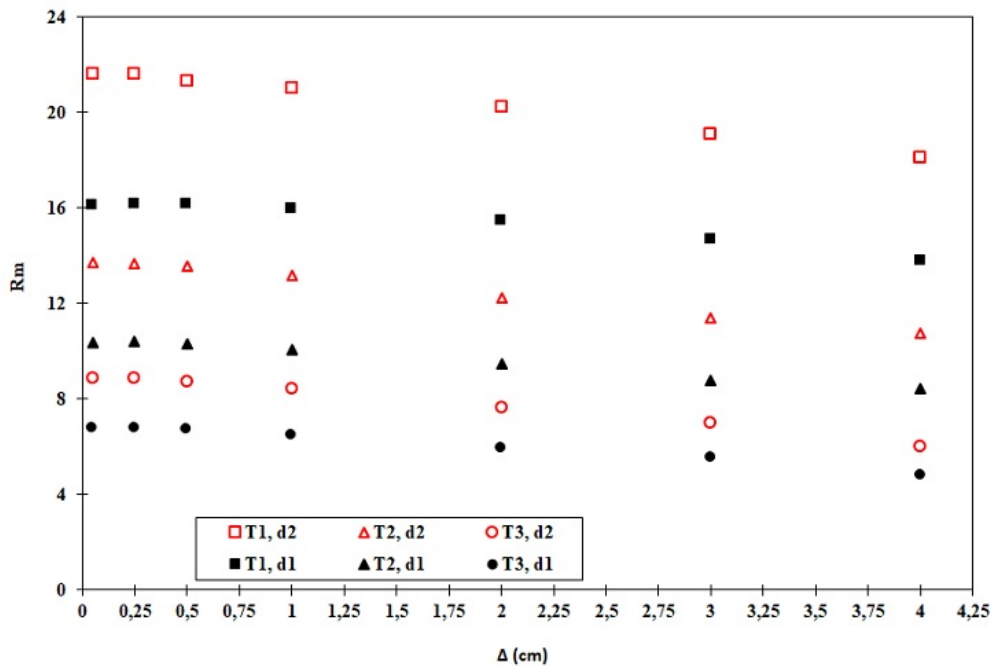

Figure 4.5: Variation in behavior of entrainment ratio for tubes T1, T2 and T3 with ideal injectors d1 and d2 and distance ranging from $\Delta=0.05$ to 4cm at $\dot{v}_{in}=1.88$ SLPM (Specifications are taken from Table 4.1).

It can be observed from Figure 4.4(a) that entrainment ratio increases for the same tube (T1) with a lower injector diameter and almost 1.35 times more than injector d1. In Figure 4.4(b), similar results were also observed when T2 tube was used and comparing with the previous case in Figure 4.3(b), primary aeration has been increased nearly 1.36 times with d2 injector. Just like previous cases in Figure 4.3, maximum value of R_m was noticed at Δ=0.5cm. In all cases, the real geometry has provided more aeration than the ideal one but the deviation increased more sharply beyond 2cm distance between nozzle and tube. Effect of injector diameter on primary burner aeration has also been supported by the investigation made by Almeida et al. [16] where similar behavior was observed.

Figure 4.5 presents that for all three tubes (T1, T2 and T3), higher entrainment of air has been found while using the d2 injector operating with same inlet boundary condition and on an average, 28%, 30% and 28% increase in entrainment ratio have been observed than the injector d1. It's worth mentioning that for all the cases which have been investigated in Figure 4.5, the ideal geometry of injector is used. Numerical investigations for other cases including combustion (hot and cold test), the ideal and simplified nozzle geometry will be used.

(a) Ideal geometry with 1mm diameter   (b) Real geometry with 1mm diameter
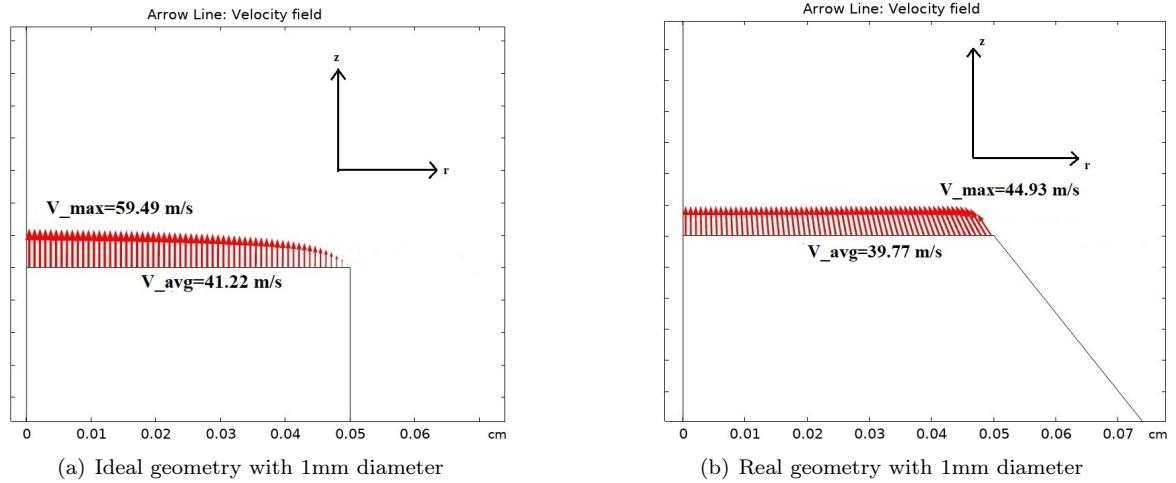
Figure 4.6: Velocity vector distribution over the top surface of 1mm injector for ideal (a) and real(b) geometries at $\dot{v}_{in}$=1.88 SLPM.

Discrepancy in entrainment ratio behavior between the ideal and the real geometry can be explained from the velocity vector distribution at injector exit. Figure 4.6(a) shows the parabolic velocity profile of the injected fluid from an ideal injector. From the maximum and minimum values of velocity distribution on the top of injector exit, it is apparent that due to high momentum transfer in the 'almost rectangular' velocity profile (with values) obtained from CFD environment for real geometry in Figure 4.6(b), the drag force increases thus dragging more surrounding air towards the mixing tube entrance. The momentum transfer is lower for the ideal injector thus it experiences a lower drag force to drive the air for entrainment. Average velocities for both cases remain almost same (around 40 m/s) though 3.6% relative difference has been found due to numerical inaccuracy. This difference is very significant as it is responsible for the deviation in results between ideal CFD geometry and real experimental results of PIV and spectroscopy. Upto a limit (Δ), the error level is small but with increase in distance, it becomes bigger which is discussed later. In section 4.4.2, a comparison is made to observe the deviation in results of between an air-air

CFD model (ideal and real case) and PIV setup with same configuration.

4.1.2 Influence of distance between injector and tube on primary aeration

In order to investigate the effect of distance between and mixing tube and injector, three tubes and two injectors have been selected. The injectors are d1 and d2 used previously and an additional tube (T3) with external diameter of 1.2 cm has been chosen. For all six cases, the inlet boundary condition remained same (v_{in}=1.88 SLPM). Considering the computational cost, seven different distances have been selected which are 0.05cm, 0.25cm, 0.5cm, 1cm, 2cm, 3cm and 4cm.
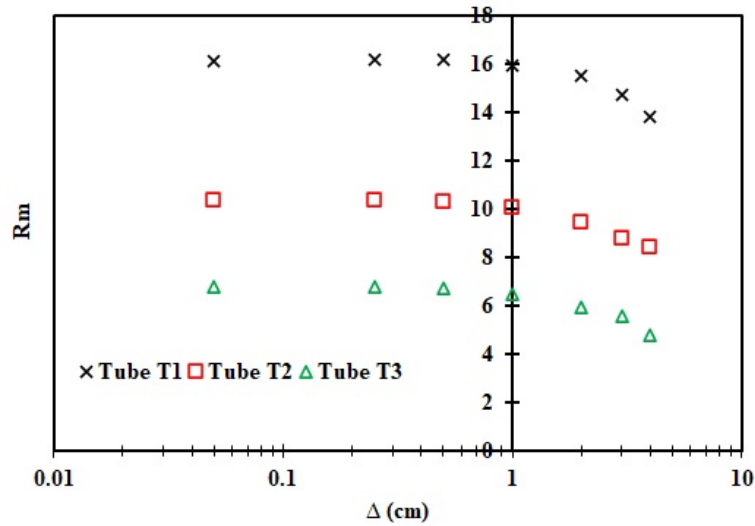
(a) Rm vs. Δ for injector d1=1mm
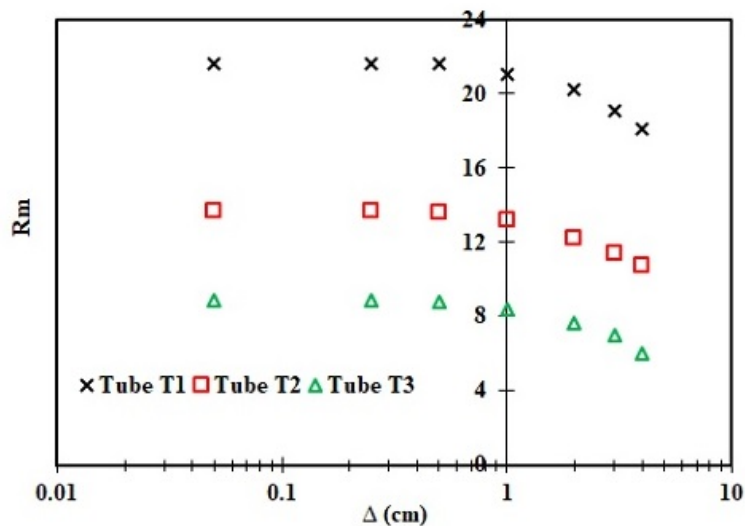
(b) Rm vs. Δ for injector d2=0.76mm

Figure 4.7: Descension of entrainment ratio from Δ= 0.25cm to Δ=4cm using ideal injectors d1 and d2 at v_{in}=1.88 SLPM.

Figure 4.7(a) shows the trends for air entrainment along with the increase in distance between tube and injector ranging from 0.05cm to 4cm for three different tubes (T1, T2 and T3). For the same injection condition i.e. same inlet boundary condition and injection diameter (d1), tube T1 has more amount of

air entrained than tubes T2 and T3. But as the distance increased, the entrainment performance also decreased. For the first four distances which range from 0.05cm to 1cm, the change wasn't significant as the deviation of entrainment from each consecutive distance didn't vary more than 2%. But for bigger distances, such as: 2cm to 4cm, there was a swift decline in the entrainment ratio and the change is almost 15% for tube T1 with distance 4cm, whereas for T2 and T3, it was around 5%.

For the injection condition with injector d2, the similar trend was observed for all the three tubes and the change was very small (around 1% to 2%) for the first four distances as shown in Figure 4.7(b). As found previously, injector d2 drags more air for all the tubes while comparing to injector d1 as for same inlet mass flow rate, it gives more injection velocity. Beyond 1cm distance, the entrainment ratio fell down significantly as the distance increased. From both investigations, it is apparent that the ejector pump system working with this specific arrangement doesn't perform well when the distance is kept more than 1cm. But the results will be different depending on the geometry of the tube as well as injector. It was also reported by [27, 48] that nozzle position is also important to entrainment ratio. These research also support that there is no fixed position for injector as well as diameter meeting all kinds of criteria for the complex characteristics of the flow as well as overall performance. Other parameters are also involved including tube diameter which has also a limit and impact as discussed in the following subsection.

4.1.3 Effect of mixing tube diameter on air entrainment

As mentioned earlier, the length of the tube remained fixed throughout the investigation. In order to observe the effect of tube diameter on entrainment ratio with respect to two different injector geometries, the external diameter of the tube was increased gradually from the original size which is 1.2cm.

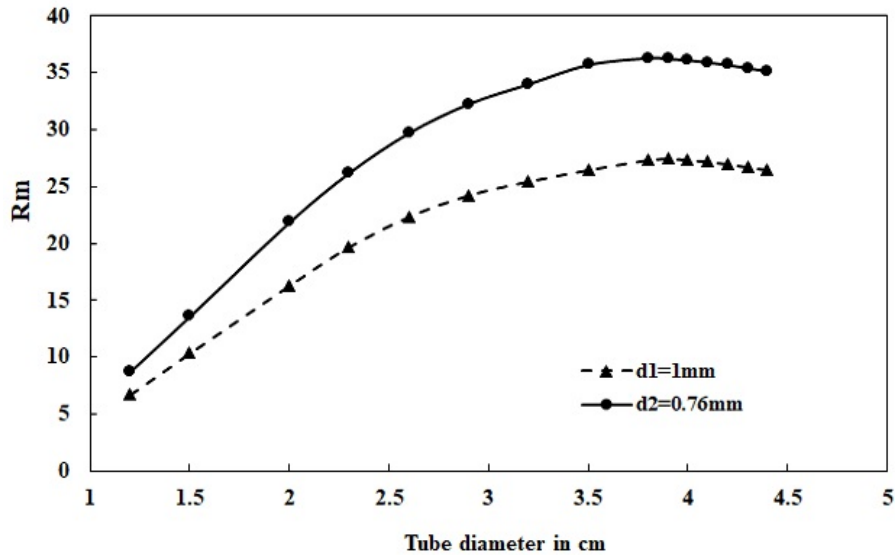Figure 4.8: Effect of tube diameter on air entrainment using ideal injectors d1 and d2 at v_{in}=1.88 SLPM.

Figure 4.8 shows the relationship between mixing tube diameter and the entrainment ratio. It can be seen that for all cases, air entrainment found to be higher for the injector d2 than that of d1. When the tube diameter changed from 1.2cm to 2cm for injector d1, difference from the consecutive cases in terms

of entraiment ratio was around 35%, which gives a sharp notification of change. As the diameter of the tube was further increased and varied between 2.3cm to 3.8cm, the difference between each consecutive cases became lower and ranged between 17% to 0.4%. Beyond 3.8cm diameter, the change was steady and the similar behavior was also found while investigating with injector d2. Almeida et al. [16] also reported the similar phenomena regarding a certain limit of increasing the tube diameter.

For all cases shown in Figure 4.8, the injector d2 gave more than 1.3 times entrainment than injector d1 and both of them exhibited the same trend with the increase in tube diameter. For this particular case with constant length of 10.1 cm and diameter of tube varied in between 1.2cm to 4.4cm, the entrainment ratio showed steady movement beyond 3.9cm tube diameter. It can be concluded that the impact of injector diameter on entrainment ratio is independent of the tube diameter, beyond D = 3.9cm

4.1.4 Effect of inlet mass flow rate on air entrainment

The mass flow rate supplied through the injector affects the performance of the ejector pump system as it is responsible for dragging the surrounding air by momentum transfer. For different positions, the behavior is different but with the increase of mass flow rate which actually governs the injection velocity, the entrainment ratio experiences a rise also. For the investigation, tube T1, T2 and T3 have been selected for both injectors d1 and d2. In order to obtain the same injection velocity from the injectors, the volume flow rates need to be varied. The following conditions presented in Table 4.2 have been chosen for the investigation.

Injection velocity	SLPM for d1	SLPM for d2	SLPM d1/SLPMd2
42.8 [m/s]	1.92	1.10	1.73
17.12 [m/s]	0.768	0.443	1.73
8.56 [m/s]	0.384	0.2218	1.73

Table 4.2: Inlet boundary conditions for two injectors.

(a) Tube T1, T2 and T3 with injector d1

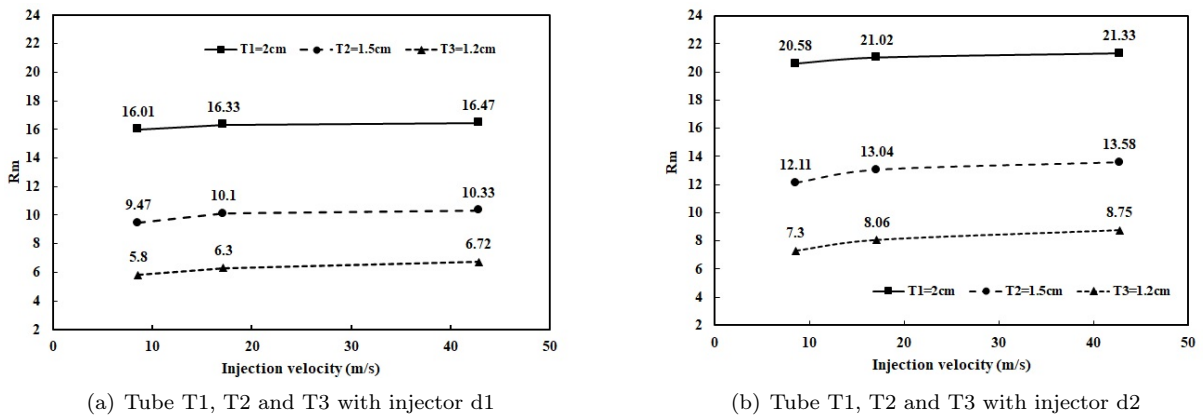(b) Tube T1, T2 and T3 with injector d2

Figure 4.9: Evolution in entrainment ratio for three tubes with three inlet conditions for two injectors working at a fixed distance of Δ=0.5cm.

The inlet conditions were chosen as per Table 4.2. From Figure 4.9(a) and (b), it is observed that amount of air entrained is increased for all three tubes with the increase in injection velocity while using

injectors d1 and d2. The distance between the injector and tube was kept at 0.5cm. While using injection velocity 17.12 m/s in injector d1, the air entrainment ratios were 2%, 6.6% and 8.2% higher respectively for tubes T1, T2 and T3 than using the injection velocity of 8.56 m/s. When the velocity of injection is increased at 42.8 m/s, entrainment ratio for all three tubes respectively experience 2.88%, 9% and 15.06% bigger values than those of 8.56 m/s, which are represented in Figure 4.9(a). Similar trends have been observed for same injection velocity for three tubes using injector d2 in Figure 4.9(b). For each respective case, the entrainment ratio was higher than the cases in Figure 4.9(a). Because the primary mass flow rate of aeration with respect to mass flow rate injection for a lower injector diameter gives a higher value than for the same ratio obtained from a bigger injector diameter. Just like previous case, 17.12 m/s injection velocity for d2 injector gives 2.13%, 7.67% and 10.41% increase than 8.56 m/s whereas comparing to 42.8 m/s injection velocity, the rise were 3.64%, 12.13% and 19.86% respectively for T1, T2 and T3 tubes. The numerical investigation thus suggests that primary aeration has a close relation with the injection mass flow rate for ejector pump burners. But for a specific distance (Δ) and a tube, increase in mass flow rate doesn't affect the performance significantly beyond a certain value and the trend becomes almost flat which can be observed from both Figures in Figure 4.9. Similar case was also studied for a self aspirating burner [12] where it was observed that the levels of primary air entrained rapidly increase with fuel gas mass flow rate at the early stage which becomes flatter in the later stages and has been validated numerically and PIV technique.

4.2   Combustion Modeling in CFD Environment

As discussed in Chapter 2, the combustion modeling takes into account of the complex physics which involves turbulent flow, transport of chemical species and heat transfer. The combustion model that has been developed will be discussed in this chapter focusing mainly on the temperature distribution and profile as well as mass fraction of different reactants and products of combustion. One very important task is to check the consistency in entrainment ratio behavior of the combustion model and comparing it to the air-air models. Additionally the difference in air entrainment due to cold test(without combustion) and hot test(with combustion) will be also observed. Different characteristics graphs establishing relationship between temperature-distance, mass fraction-distance will be discussed. In all cases, the ideal injector geometry has been used along with tube T2 made of stainless steel. The combustion model presented here has been developed by using one step propane combustion mechanism. Later two cases considering two step mechanism will be given to observe CO emission and equivalence ratio.

$$C_3H_8 + 5O_2 \longrightarrow 3CO_2 + 4H_2O \tag{4.3}$$

4.2.1   Observation of consistency in the behavior of combustion model entrainment ratio

The parametric study provided important insights regarding ejector pump operation. With the combustion model implemented considering chemical kinetics as well as heat transfer, it is important to check

the system's consistent behavior along with the change of different parameters. In order to verify that, an inlet condition of 0.806 SLPM has been chosen for ideal injector d1 and d2 for tube T2. The distance between tube and injector varied between $\Delta=0.25$cm to $\Delta=2$cm. Considering the high computational cost only four distances have been selected for each injector.
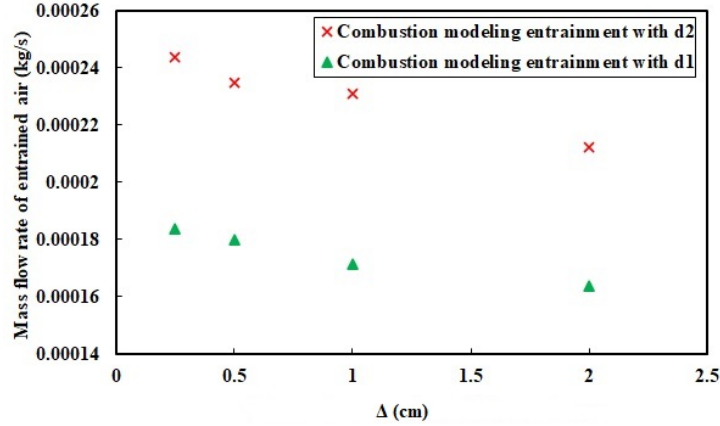

Figure 4.10: Variation in combustion model entrained air mass flow rate for injector d1 and d2 for distances $\Delta=0.25$cm to 2cm at $v_{in}^{\cdot}=0.806$ SLPM.

Figure 4.10 gives the decreasing trend of entrained air mass flow as the distance (Δ) increases. As expected, which is observed from previous studies, injector d2 gives more amount of entrained air for same inlet mass flow rate condition. In an average, amount of air entrained with d2 was found to be 30% higher than injector d1. Also, fall in mass flow rate value is around 3% for lower distances such as 0.25cm and 0.5cm. With increase in distance, the difference becomes bigger and reaches approximately 6% to 8%.

4.2.2   Effect of hot test and cold test on primary aeration

Among different methods for validating the numerical model, one of the effective methods is to validate the physics of primary aeration during hot test and cold test. In this method, numerical model validation was carried out in two stages: Cold flow validation by deactivating the *Non-isothermal Flow* physics in CFD environment and in second phase, the hot flow validation was done by activating *Non-isothermal Flow* physics and making a premixed combustion at the top of the tube. During both flow tests, the inlet temperature of fuel was kept at 298K. It should be mentioned also that other physics such as *turbulent flow* and *transport of concentrated species*, were activated all the time during the simulation period. The operating parameters for the both test are set according to Table 4.3.

Parameters	Values
Inlet volume flow rate	0.806 SLPM
Tube	T2
Injector	d2
Distance (Δ)	0.25cm to 2cm

Table 4.3: Setup specification in numerical model for cold and hot test.

It can be observed from Figure 4.11 that there's a significant difference in terms of primary aeration
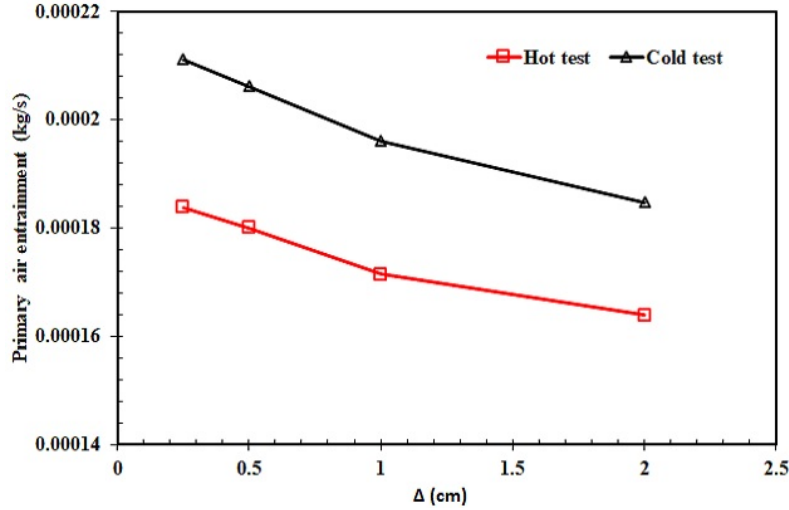
Figure 4.11: Discrepancy and trend of primary air entrainment during hot test and cold test at $v_{in}=0.806$ SLPM.

while performing the computational investigation in hot flow test and cold flow test. In almost all cases, 14% more primary aeration has been achieved during the cold test. The preheating effect caused by combustion is responsible for lower primary air entrainment. During the hot test, due to rise in temperature of the burner, the temperature of the fuel air mixture flowing through the mixing tube increases, thus leading to lower density and higher velocity. Consequently, there's higher pressure drop across mixing tube ports and causing a low primary air entrainment for the hot test comparing to the cold one. The difference between the buoyancy and the weight of the fluid inside the mixing tube increases during hot test due to decrease in density of the fluid causing weight reduction. Thus higher pressure drop at the burner ports due to higher temperature and lower density causes reduction in suction of the primary air. In an investigation on a self aspirating burner, Namkhat and Jugjai [12] observed the effect of changes in the combustion air temperature on the primary aeration. It was also found that the level of primary aeration decreased with an increasing preheated air temperature. It gives a good remark and insight regarding burner design (mixing tube) in order to get an accurate information regarding primary air entrainment.

4.2.3 Estimation of equivalence ratio for different injectors (d1,d2) with increasing distance (Δ)

Combustion models have been developed using one step reaction mechanism for two injector sizes (d1,d2) and tube T2 with an external diameter of 1.5cm. Here the purposes is to estimate the equivalence ratio (ϕ) and to observe the effect of injector diameter and distance between tube and injector (Δ). A volume flow rate of 0.806 SLPM has been chosen which gives two different injection velocity, 18.11 m/s and 31.36m/s respectively for injector d1 and d2. The ideal geometry of the injector was selected to carry out the computation.

It is evident from Figure 4.12 that equivalence ratio is strongly influenced by the size of the injector as well as the distance between mixing tube and injector. Using a bigger diameter injector (d1), gives
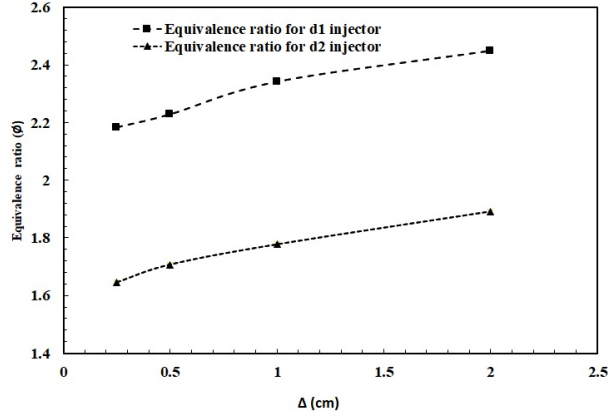
Figure 4.12: Evolution in equivalence ratio for two injectors d1 and d2 with variation in distance from Δ=0.25cm to 2cm at $\dot{v}_{in}$=0.806 SLPM.

less amount of primary aeration when compared to the primary aeration caused by smaller injector (d2). From parametric study, it was found that with the increase in distance, entrainment ratio decreases and as a result, the equivalence ratio also rises, taking the flame towards rich or more rich condition. Due to the injector diameter difference, a discrepancy level of approximately 30% was observed between the equivalence ratio obtained from two cases. It is interesting to notice that lower injector diameter takes the mixture to towards leaner condition as the high velocity induces the surrounding air to enter the mixing tube entrance due to momentum transfer. Duarte's [49] investigation gives also a clear similar indication regarding the influence of distance (Δ) and injector diameter on equivalence ratio.

4.2.4 Temperature, mass fraction and velocity vector distribution for a single combustion model

Using an inlet volume flow rate of 0.806 SLPM for injector d1, which gives an injection velocity of 18.11 m/s, tube T2 has been used at a fixed distance of Δ=0.5cm. It was aimed to observe the flame temperature and its evolution along with the distribution of mass fraction of different reactants and products. The schematic diagram for temperature measurement technique is presented in Figure 4.13. A K type thermocouple has been used in order to measure the flame temperature using *QuickDAQ* data logging system. The sample rate was kept at 100 Hz, and at channel *DT9828(01).Ain 0*.

Figure 4.14 depicts the experimental visualization of the flame supported by numerical results from the modeling. From Figure 4.14(a), the flame developed due to premixed combustion in the ejector pump burner can be seen. As expected, different flame zones are visible with inner zone temperature being lower than the outer zone [50]. The surrounding area around the inner flame structure at the reaction zone exhibited the highest temperature as soon as the ignition occurs. As the flame is developed in a conical shape shown in Figure 4.14(b), the temperature along the core also increases whereas the flame temperature along vertical direction from the mixing tube edge gradually decreases. Trends of temperature are plotted in Figure 4.14(c) with the data obtained from CFD environment. The flame height was nearly 12 cm in experiment and similar flame structure has also been observed from the numerical modeling.
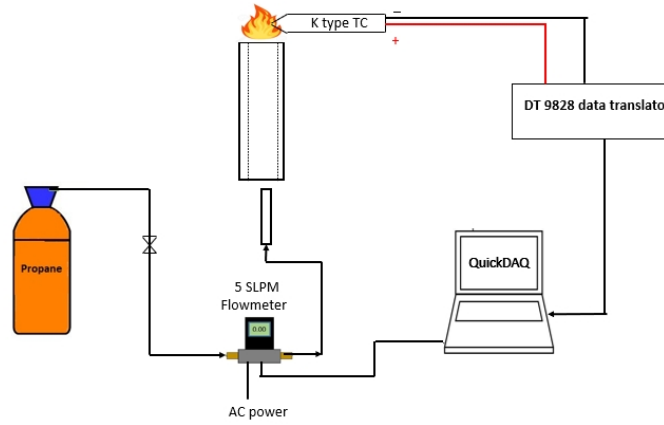
Figure 4.13: Temperature measurement of tube T2 with ideal injector d1 at a distance of $\Delta = 0.5cm$.
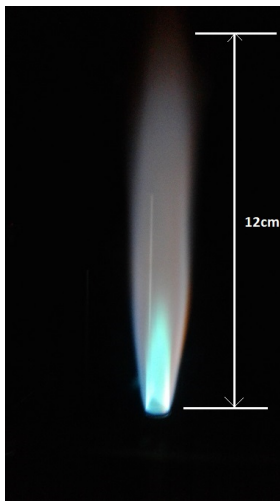
(a) Photograph of flame with specified setup
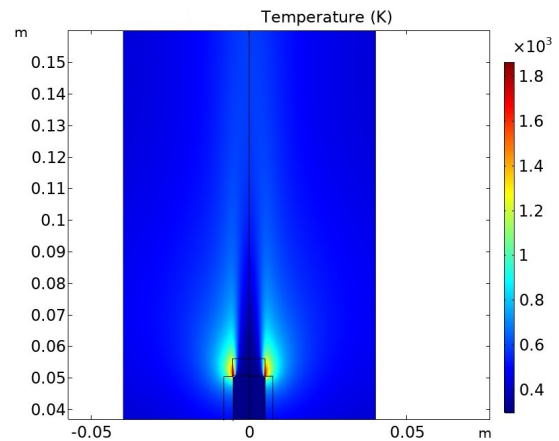
(b) Temperature development contour of flame
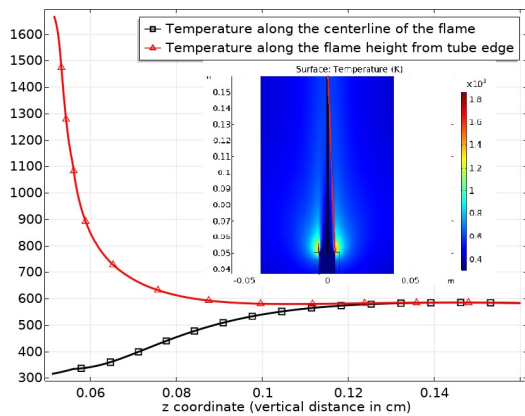
(c) Temperature distribution along z co-ordinate
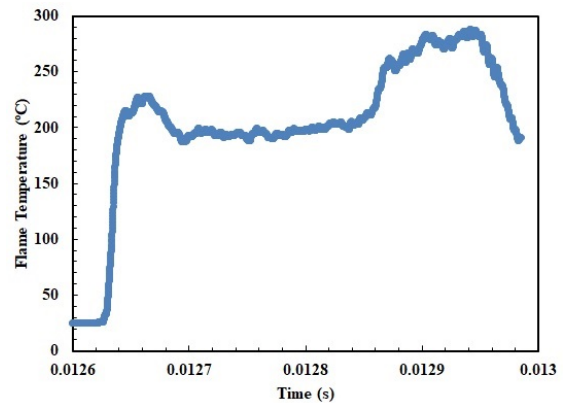
(d) Temperature acquired by K type thermocouple using *QuickDAQ*

Figure 4.14: Flame photograph(a), temperature profile(b,c) from CFD and data acquired by thermocouple in *QuickDAQ* environment(d) for an inlet condition of 0.806SLPM, injector d1, tube T2 and Δ=0.5cm.

The temperature of the flame at a height of 5 cm from the tube surface was measured as 565K (Figure 4.14(d)) whereas the numerical modeling shows around 530K in the same position. Tieng et al. [51]

43

investigated the whole field temperature distribution of a laminar, axisymmetric, propane air, lean flame measured by interferometric technique where the temperature distribution was observed at different flame height showing a deviation in the distribution profile. Flame profiles from other configurations (different Δ) are given in appendix A.

Mass fraction distribution

In one step reaction mechanism, propane and oxygen have served as the reactants whereas water and carbon di-oxide were the products. The distribution of mass fraction needs to be consistent and it's one of the ways to validate the model. In a complete combustion, the fuel and oxidizer are expected to be fully depleted and the mass fraction of the products should achieve a nominal value. The purpose of presenting these characteristics graphs is to show that the numerical model is resembling the actual cases even though one step reaction mechanism is being used. For further investigation multi step mechanism can be implemented.

(a) Mass fraction of C_3H_8

(b) Mass fraction of O_2

(c) Mass fraction of CO_2

(d) Mass fraction of H_2O
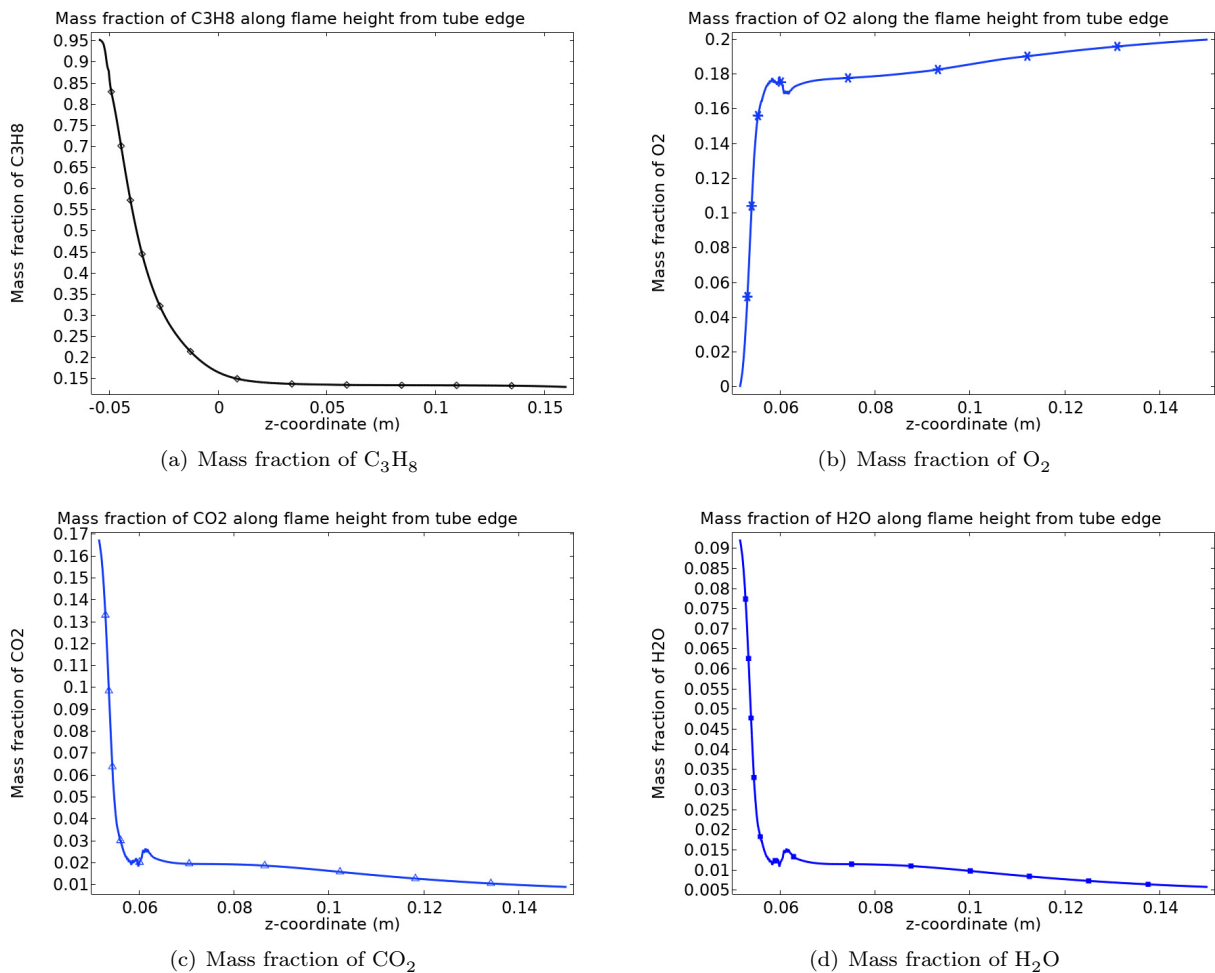
Figure 4.15: Mass fraction of different chemical species for an inlet condition of 0.806SLPM, injector d1, tube T2 and Δ=0.5cm.

Figure 4.15(a) shows the depletion of C_3H_8 from the injection towards combustion. From the coordinate position it is seen that the mass fraction of C_3H_8 initially remain unchanged. But as it was mixed with the air during the entrainment and the mixture traveled along the tube height, the mass fraction

decreased. At the position of 0.05m from CFD modeler interface, the combustion starts at the top of tube surface. Subsequently, the amount of C_3H_8 was lowered as the flame is developed. For O_2, the mass fraction was considered in the surrounding air as 0.23. At the beginning of combustion the O_2 present in the fuel air mixture was depleted. But later with the flame development, more O_2 from surround air joined and thus at the top height of flame along the linear positive z direction from tube edge, the mass fraction almost becomes equal to the original amount in the ambient air which is depicted in Figure 4.15(b). For the products of combustion CO_2 and H_2O, presented respectively in Figure 4.15(c) and Figure 4.15(d) the initial mass fractions from the reaction zone start to decrease along the flame height. Both of them experience a slight jump as the exit the reaction zone in the modeling environment as they are joined by surrounding air's molecule containing little amount of H_2O and CO_2.

CO emission and equivalence ratio

In order to observe the behavior of CO emission with the increase of equivalence ratio, two combustion models considering two step reaction mechanism have been developed. The distance between tube and injector was varied whereas the injection volume flow rate was kept same. The reactions take place in the following order.

$$C_3H_8 + 3.5O_2 \rightarrow 3CO + 4H_2O \tag{4.4}$$

$$CO + 0.5O_2 \rightarrow CO_2 \tag{4.5}$$

(a) Mass fraction of CO for Δ=0.5cm

(b) Mass fraction of CO for Δ=1cm
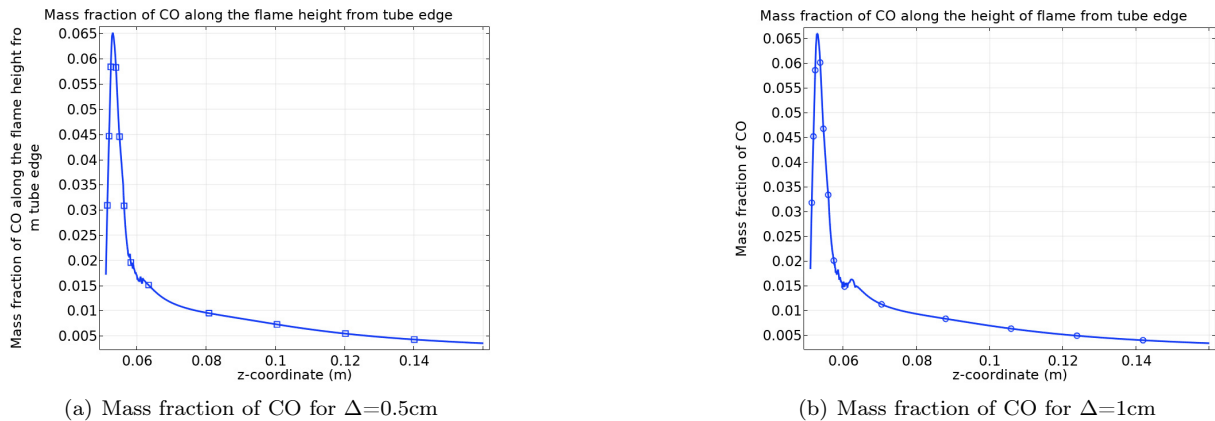
Figure 4.16: Distribution of CO using tube T2, injector d1 and two distances, Δ=0.5cm and 1cm.

With the presence of fuel during an incomplete combustion, amount of CO starts to increase. In case of low amount of oxidizer i.e. low amount of aeration, the amount of equivalence ratio increases as the fuel remains high due to the absence of sufficient oxidizer. From parametric study in section 4.1.2, it was observed that entrainment ratio which is a function of primary air entrainment, decreases when the distance (Δ) increases. Even though the amount of CO in very low in the atmosphere (in level of parts per million) but it's one of the major pollutants during combustion. Figure 4.16(a), which is a setup with Δ=0.5cm that causes more aeration, shows that the amount of CO starts to increase in the first stage of combustion as it stayed just below 0.065. With the supply of more air, it starts to decrease as combustion

continues to occur. But for a distance of Δ=1cm, presented in Figure 4.16(b), the value of CO slightly goes above 0.065 as the case has now moved to more rich condition with the increase of equivalence ratio. Ishak and Jaafar [52] showed CO emissions with equivalence ratio for different orifice plate diameter. It was observed that with smaller area ratio of orifice plate produce better emission reduction and on the opposite, amount of CO increases with the increase in equivalence ratio.

Velocity vector distribution during entrainment for hot and cold test

Apart from the primary aeration, secondary aeration also takes place at the flame region (top of the tube) due to drag effect. As found earlier, due to difference in fluid density due to preheating effect, cold test gives more primary aeration that the hot test. Similarly, secondary aeration amount also decreases for a hot test case. The velocity vectors are given in the following Figure 4.17 representing primary and secondary aeration for both hot and cold test.

(a) Primary entrainment during hot test

(b) Secondary entrainment during hot test

(c) Primary entrainment during cold test

(d) Secondary entrainment during cold test
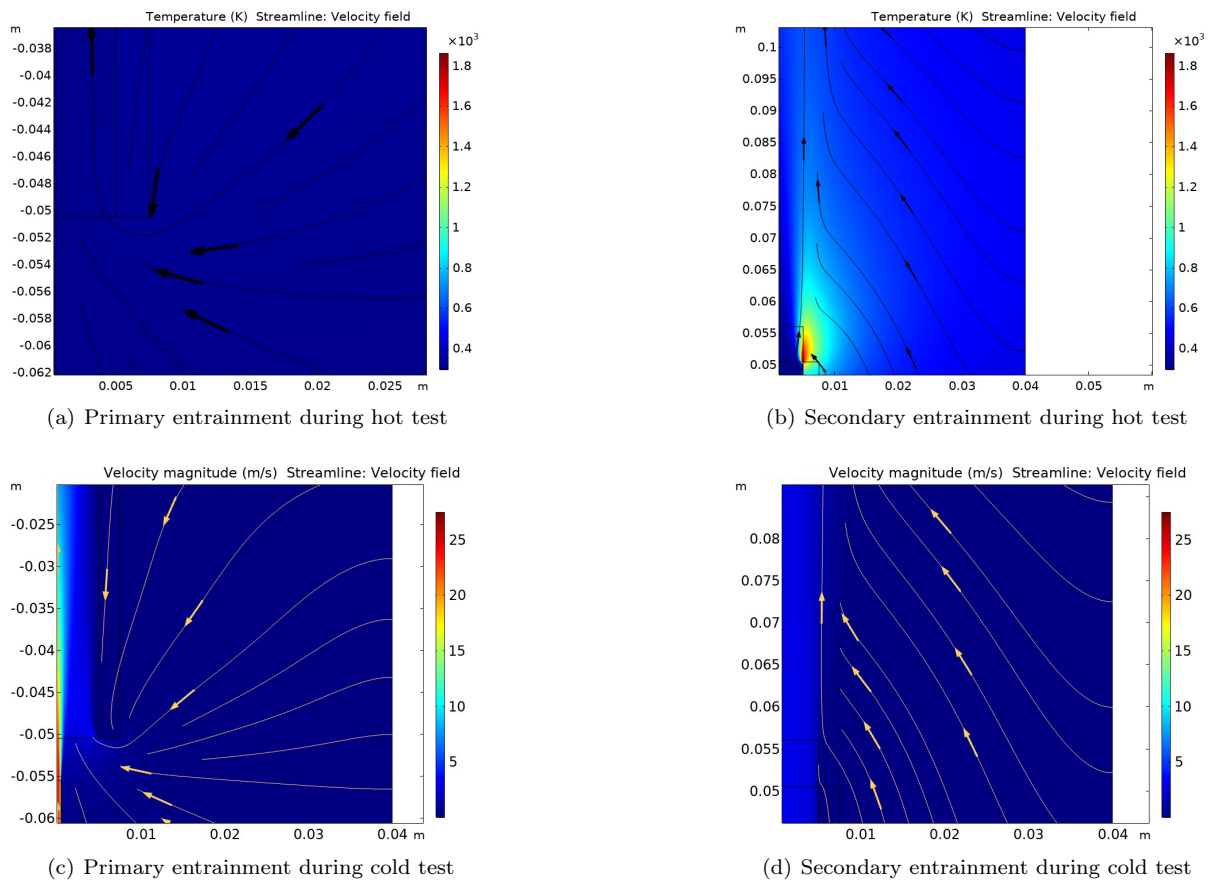
Figure 4.17: Vector profile of primary and secondary aeration during hot test (a,b) and cold test (c,d) with tube T2, ideal injector d1, inlet volume flow rate of 0.806 SLPM for a $\Delta = 0.5cm$.

For the same configuration in the CFD post processing environment, the velocity vectors appear to be denser for a cold test than a hot test condition both for primary and secondary air entrainment.

Temperature distribution along the tube wall

The stainless steel type 304 tube wall has a conductivity of 14.4 W/mK at a temperature of 20 degree Celsius [53]. Due to the flame development, the conduction heat transfer occurs along the tube wall which has a thickness of 0.25 cm. This phenomena plays an important role on aeration. The temperature at the tube top edge was found to be highest than any other region of the tube. Figure 4.18 shows the behavior of temperature profile along negative z coordinate (from tube upper part towards lower part). The temperature at the lower region near entrainment was found to be around 52 degree Celsius.
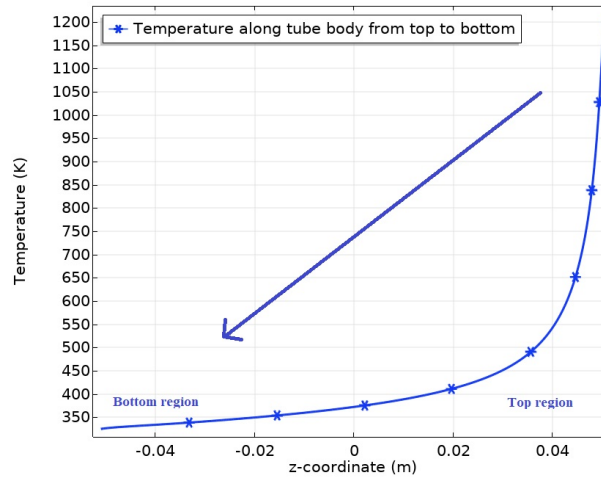

Figure 4.18: Declination of the temperature along tube wall towards primary entrainment region.

4.3   Analysis of Results from Chemiluminescence Spectroscopy

The detailed experimental setup of chemiluminescence spectroscopy has been described in subsection 3.1.1. After setting up the experimental setup, system calibration has been performed in order to generate calibration curves which will later be used for estimating equivalence ratio by taking the ratio of different chemical species into account. In order to correlate the measured values of intensities emitted by the radicals to the equivalence ratio, which have been acquired during the chemiluminescence technique, generating a calibration curve is essential which was developed in Figure 3.5. Its main purpose is to ascertain a proper correlation by performing the analysis of the chemical species radiation emissions of a reference flame with a known equivalence ratio.

Several conditions have been tested and the equivalence ratios are evaluated from the obtained results. Different injection mass flow rates have been set for three different tubes working with the injector d2. The mass flow rates varied for all the tubes as they were selected based on the stability limit (flashback and blow-off) of flames uniquely identified for each tube. The three tubes are named as T4, T5 and T6.

Using the relationship from Equation 3.3, the equivalence ratio is calculated for the arrangements mentioned in Table 4.4. It was decided to investigate three tubes with a fixed injector by using three different injection conditions. It must be mentioned that the injector position was maintained almost at the entrance of the tube (at $\Delta= 0.05$cm). Certainly the injector position has an impact on the equivalence

Tube	L (cm)	D (cm)	d (cm)	t (cm)	SLPM	Material
T4	15	1.9	0.076	0.25	0.6	Copper
	15	1.9	0.076	0.25	0.8	
	15	1.9	0.076	0.25	1	
T5	31	1.9	0.076	0.2	1.2	Copper
	31	1.9	0.076	0.2	1.4	
	31	1.9	0.076	0.2	1.45	
T6	8	1.7	0.076	0.3	0.8	Brass
	8	1.7	0.076	0.3	1.2	
	8	1.7	0.076	0.3	1.4	

Table 4.4: Tube, injector and injection conditions for tested spectroscopy cases.

ratio but in these investigations, the main objective was to generate the calibration curves and checking their applicability for successfully determining the equivalence ratio. Later, one of these three cases will be compared with the similar combustion model developed by CFD simulations.
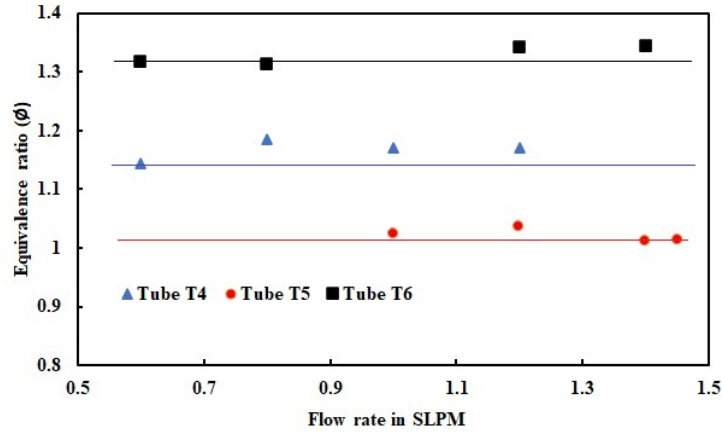

Figure 4.19: Equivalence ratio obtained from spectroscopy for different tubes.

Figure 4.19 shows the behavior of the equivalence ratio for three different tubes operating under different injection conditions in terms of mass flow rate but the injector diameter remains same. For all three cases, it's clearly visible that there's no significant variation in equivalence ratio even though the mass flow rate of the fuel has been changing for a fixed injector position. Tube length has also impact on entrainment ratio as increasing L implies and increase of R_m and, therefore a decrease of ϕ. Variation among the equivalence ratios didn't change more than 2%. In an investigation performed by Duarte [49], it was reported that varying the fuel mass flow rate while maintaining the injector diameter leads to constant equivalence ratio. As a result, the entrainment ratio is independent of the fuel mass flow rate, for a value of $\Delta = 0.05$cm keeping unchanged all the other parameters, namely, L, D, d which is supported from previous research also [24].

4.4 Analysis of Results from Particle Image Velocimetry

After setting up the experimental setup and the data acquisition, the third essential part for PIV is the post processing that involves the image analysis. A number of procedures can be performed before and after in order to correlate the data of the particle image pairings. But in this case, no pre-image filtering

correlation was applied. Rather, image masking has been used to identify and fix the area of interest during the investigation.

For performing the correlation, several approaches each with different characteristics are followed. But depending on the flow, setup and particle seeding condition, the approach can be different. A technique known as cross correlation offers a way to calculate 2D velocity vector field from the captured image pair. It's a spatial analysis where the entities are studied based on their geometry and specifically better suited for flow with a strong particular direction [54]. The approach correlates the light intensity emitted by the seeding particles from the time of first exposure (t) to the second one (t+Δ t) sequentially. As a result, the displacement of the particle can be obtained by a peak detection method. To post process the data in this work, another method named as "Average Correlation" has been used. Here, the correlation function from each interrogation area is averaged for all the images at each location. It's a robust technique proven to be useful in applications where it's hard to maintain a uniform particle density over the entire acquisition period. The average correlation method performs better than other method and producing less than 0.5 to 1% erroneous measurements [46]. For studying the entrainment, the average correlation along with a large number of acquired image pairs was selected over the specific cross correlation of each pair and vector map averaging.

Interrogation area (IA)and pulse timing (Δt) between two consecutive laser shots are extremely important parameters to be set during the experiment which greatly affect the post processing output. IA determines the subdivisions of the main image frame into n x n pixels. A single mean velocity vector for each IA is generated which is found by individually analysing both laser pulses. Distance travelled by the particle, time difference between two pulses are connected with the chosen dimension of the IA. These three values must be adjustable in such a way so that the clear movement of the particle from one frame to another is easily obtained without missing the particle. When the time between pulses is very small, the particle will have a small displacement than the required in order to have a proper velocity vector. As a matter of fact, for a high velocity, small time difference would be appropriate when the IA remains constant. If the time different is too large, the particle will have large displacement and it might escape from the IA frame. The particles acquired near the IA border can still be lost from the frames. even though with a proper value of time difference and IA dimension. A parameter called overlapping factor estimates the nearby interrogation approximates neighboring interrogation areas which facilitates more vectors in both plane direction. In this experiment, 50% x 50% of overlapping factor has been used. Table 4.5 contains the parameters which have been set in PIV platform.

PIV parameters	Configured options in *Dynamic Studio*
Correlation technique	Average correlation
Size of IA	$64 \times 64, 64 \times 128$
Time between pulses (Δt)	60 μs
Image pairs in each recording	200
Overlapping factor	50% $\times$50%

Table 4.5: PIV setup configurations in *Dynamic Studio* environment.

The velocity vectors are derived from sub-sections of the target area of the tracing particle seeded flow by measuring the movement of particles between two light pulses and can be mathematically expressed
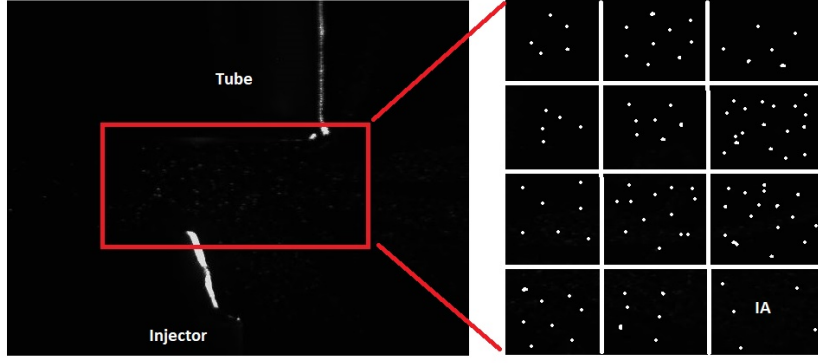
Figure 4.20: Subdivisions obtained for interrogation area from one frame.

as:

$$\bar{v} = \frac{\Delta \bar{x}}{\Delta t} \tag{4.6}$$

Where, $\bar{v}$, $\bar{x}$ and t respectively represent average velocity, displacement and time. The IA areas from each image frame denoted as I_1 and I_2 are cross correlated with each other, pixel by pixel. After the correlation, a peak signal has been produced denoted as dX and further measurement of displacement as well velocity is performed by sub pixel interpolation. Thus cross correlation is a function of IA, distance from target area to camera lens s and distance between particles X.

$$C(s) = \iint_{IA} I_1(X) \cdot I_2(X - s) dX \tag{4.7}$$

Due to the nature of the injection flow as well as flow of during entrainment, the occurrence of a particle out of the plane can create sudden absence of particles between two frames. Adjusting the power of the laser and focal length, a thicker laser sheet can be produced. But it may also create reflection in the adjacent metal structures thus producing problem to the camera lens as well as giving erroneous vectors. But during the experiment, laser sheet thickness was kept at the minimum and the data acquired were analyzed after proper range validation.

4.4.1 Post processing of raw PIV data for obtaining mass flow rate and velocity profile of air entrainment

The raw PIV data for each test case was imported in the form of .csv file which has been processed by *MATLAB* script in order to obtain the mass flow rate of air entraiment as well as the profile. Just below the bottom line of the tube, the coordinates from the captured frame are detected and based on that, the data have been filtered by excluding those which are not of interest. A radial coordinate system is developed to define the position of each velocity vector and to perform the surface integration in order to calculate the mass flow rate of entrainment.

The surface integral formula for the mass flow rate of entrained air considering the positive y axis velocity component along a radial distance of R over a circular cross sectional area of A (unit:m^2) can

be defined as:

$$\dot{m} = \iint \rho \vec{V} \cdot d\vec{A} = \int_0^{2\pi} \int_0^R V_a r \, dr \, d\theta \qquad (4.8)$$

Where V_a is the velocity component in positive y direction in m/s, ρ is the mass flow rate of air in kg/m^3.
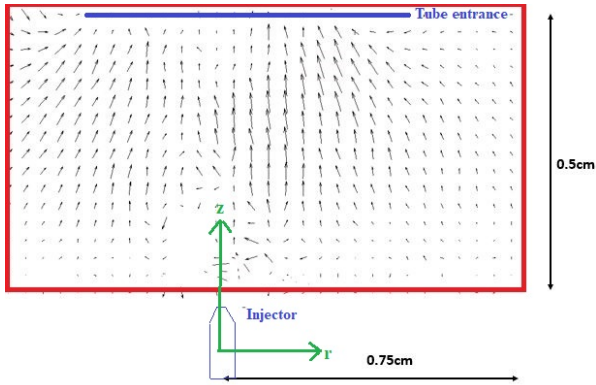
(a) Velocity vector for Δ=0.5cm
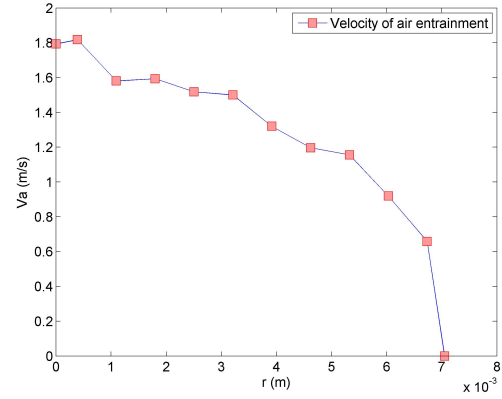
(b) Entrainment profile for Δ=0.5cm
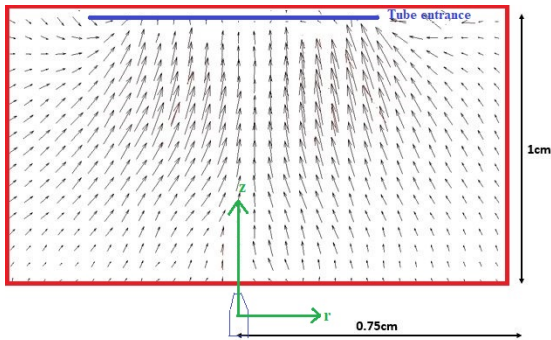
(c) Velocity vector for Δ=1cm
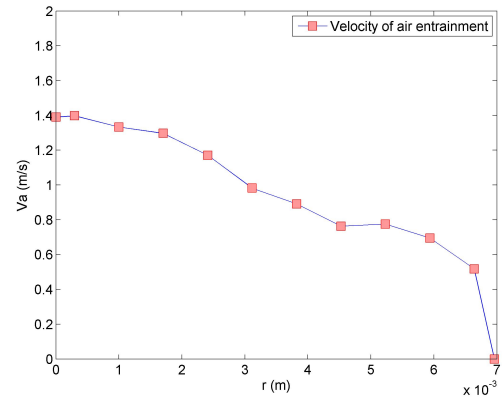
(d) Entrainment profile for Δ=1cm
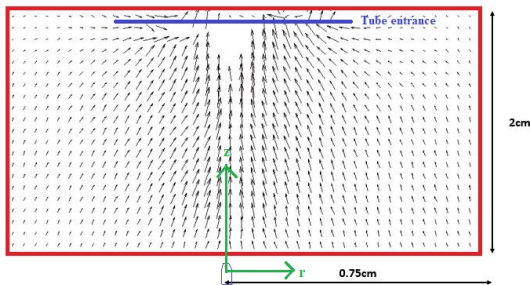
(e) Velocity vector for Δ=2cm
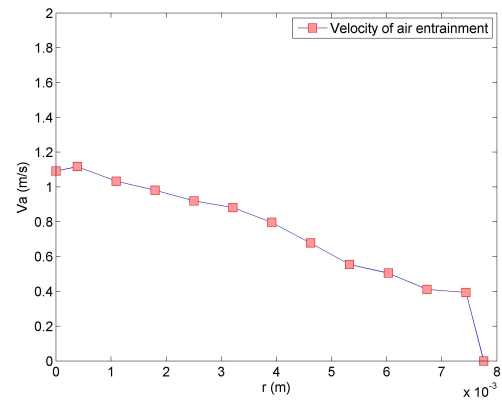
(f) Entrainment profile for Δ=2cm

Figure 4.21: Velocity vector ((a), (c), (e)) and development of air entrainment profile ((b), (d), (f)) through the bottom of T2 tube along radial distance for Δ=0.5cm, 1cm and 2cm using injector d1 and $\dot{m}_{in}$=0.806 SLPM.

51

Figure 4.21 shows the velocity vector distribution and profiles for different distances (Δ) at a mass flow rate of 0.806 SLPM. In Figures 4.21 (a,c,e), the positions of the tube entranae and injector have been marked as the air is dragged towards tube entrance. As supported from the air-air approach described in section 4.1.2, the velocity of entrainment which consequently affects the mass flow rate of entrained air decreases as the distance (Δ) increases. The parabolic profiles from in Figures 4.21 (b,d,f) suggest that the seeding particles dragged towards the tube achieve the highest velocity near the entrance of the tube. To obtain the velocity vectors, the range validation technique has been used in order to remove the erroneous vectors. Few erroneous vectors appeared in the processed data due to the movement caused by high injection velocity of propane.

4.4.2 Discrepancy in entrainment ratio using air-air approach from PIV setup and CFD design (real and ideal)

It was discussed earlier in section 4.1.1 that the discrepancy between the entrainment ratio obtained for real and ideal injectors occurs due to the difference in geometry. The PIV technique used an injector (d1) of real shape and experiment has been performed to investigate the entrainment ratio in order to compare with the results from CFD environment.
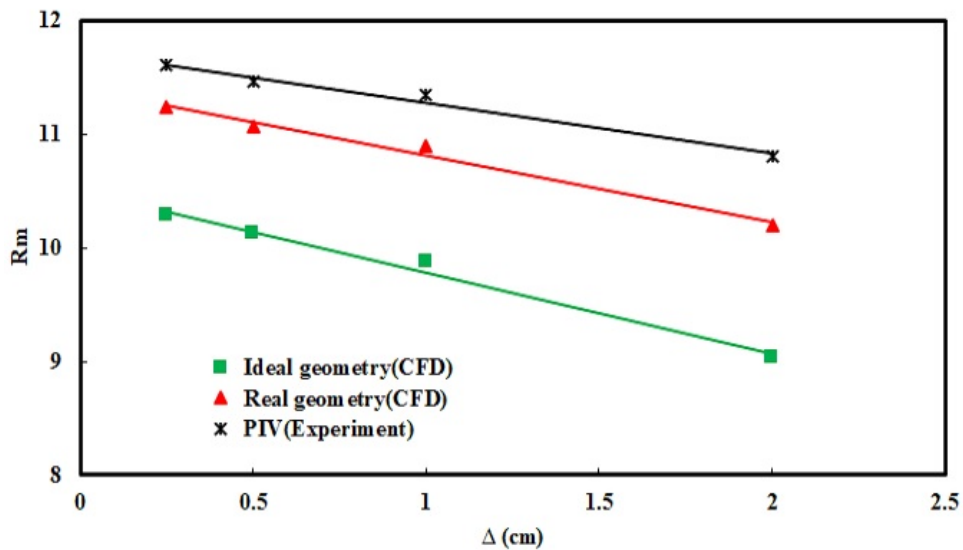
Figure 4.22: Observation of entrainment ratio discrepancy between values from CFD environment (ideal and real injector) and PIV with real injector at v_{in}=0.806 SLPM.

Figure 4.22 depicts the trend of entrainment ratio obtained from numerical modeling and experimental technique for an inlet condition of 0.806 SLPM with tube T1 and injector d1 (injection diameter 1mm). Previous numerical results show that higher entrainment ratio is observed for real geometry than the ideal one due to higher momentum transfer. As a result, the velocity as well as mass flow rate of entrained air is increased. For this specific test condition with air as working fluid, the difference between the real and ideal geometry was found to be around 9% when the distance Δ was 0.25cm and 0.5 cm. With the increase in distance, error level rises and reached upto 12% when Δ=2cm.

On the contrary, the difference between results from PIV and ideal geometry started with a discrepancy level of 12% when Δ=0.25cm. As the distance increases, the error level grows bigger and for a distance of Δ=2cm, the difference was found almost 19%. While using the real injector design, the PIV shows a close matching with the numerical results. For Δ=0.25cm and 0.5cm, it accounted for only 3.5% of error. With the increase in distance, the error level rises slightly but it was limited within 6.5%. This can also explain the difference between CFD and non-intrusive diagnostic test results while estimating equivalence ratio to be discussed later on. Thus, it is expected that further investigations through numerical modelings using the real injector geometry, the outcome will most likely to match with experimental investigations with slight error.

4.4.3 Uncertainty analysis of PIV

All experimental apparatus can give results which are deviated from the actual or the theoretical value. Errors in PIV measurement can be generated due to errors caused by system components, errors due to flow and evaluation technique [55]. For quantifying the uncertainty associated with the PIV velocity measurements, values from filtered .csv file have been used to obtain the velocity profile shape along a radial co-ordinate with injector d1 and 0.806 SLPM flow rate. The theoretical parabolic profile was plotted Figure 4.23 to observe the discrepancy from the measured data.
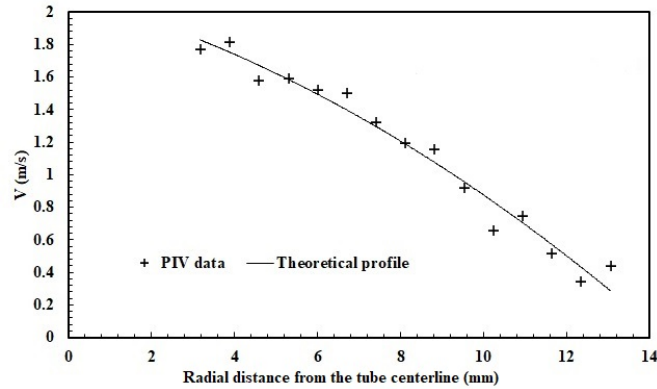
Figure 4.23: Uncertainty analysis for PIV with a flow condition of $\dot{m}_{\mathrm{in}}$=0.806SLPM and Δ=0.5cm.

The following equation stands for the Root Mean Square Error (RMSE) between the observed actual values from experiment and the theoretical values.

$$RMSE = \sqrt{\frac{\sum_{i=1}^{n}\left(\hat{y}_i - y_i\right)^2}{n}} \tag{4.9}$$

Where, $\hat{y}_i$ is the observed value, y_i is the theoretical value and n is the sample number. Using the Equation 4.9, the RMSE has been calculated as 0.06m/s and the maximum level of discrepancy with respect to the theoretical parabolic profile was found to be 24.52%. This maximum value of error occurred when the flow starts to develop for the entrainment at the coordinate which is the intersection of horizontal line to positive x direction from injector (+ r coordinate) and the vertical line towards negative y direction (- z coordinate) from the tube edge. For the whole velocity profile, the average deviation was

53

around 5%.

4.5   Comparison of Equivalence Ratio from CFD with Chemiluminescence Spectroscopy and PIV

One of the main objectives of this thesis work is to observe and understand the physics of air entrainment as well as to estimate the equivalence ratio (ϕ). For that purpose, equivalence ratio obtained from CFD modeling have been compared with the values from Chemiluminescence Spectroscopy and PIV. This is the most reliable way to validate both experimental and numerical work. Due to the use of ideal injector shape in CFD modeling environment, it is expected to have a certain level of discrepancy between the values of CFD and non-intrusive diagnostic techniques.

4.5.1   Comparing equivalence ratio from CFD combustion modeling and corresponding PIV setup

Considering computational cost, four combustion models have been computed in order to compare with the PIV. Injector d1 was used with the ideal shape and T2 mixing tube was chosen which has a length of 10.1cm and external diameter of 1.5cm with 0.25cm thickness. Four distances were used, Δ=0.25cm, 0.5cm, 1cm and 2cm. The inlet condition was chosen as 0.806 SLPM which gives an injection velocity of 18.11 m/s. The combustion mechanism is one step propane combustion mechanism.

For the PIV, the similar setup from CFD was used for the investigation. Data have been taken with flame developed for 0.806 SLPM inlet condition for the four aforementioned distances.
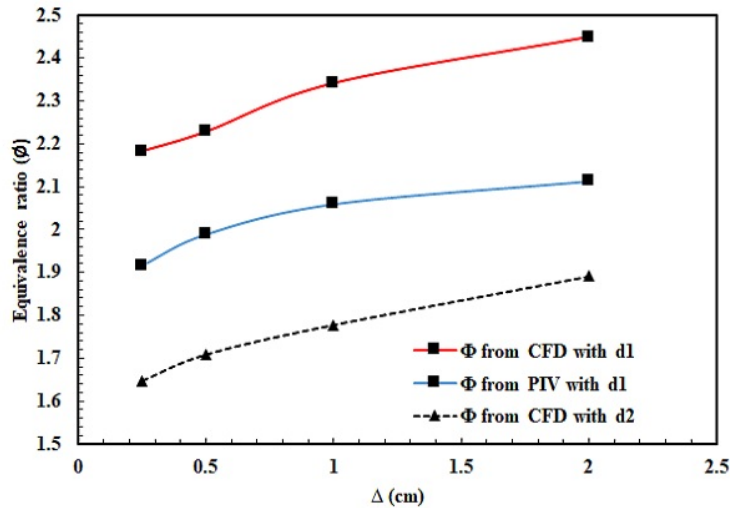
Figure 4.24: Graphical representation of the equivalence ratio derived from CFD (injector d1 and d2) and PIV (injector d1) for tube T2, and distance Δ=0.25cm, 0.5cm, 1cm and 2cm at v_{in}=0.806 SLPM.

Figure 4.24 depicts the trend of equivalence ratio with the increase in distance between tube and the injector, for both CFD and PIV technique. Investigated in the earlier sections, the air entrainment ratio decreases with the increase in the distance. It means lower primary aeration gives rise to the equivalence

ratio thus making the mixture more rich. As a result, proportional relationship has been observed between the distance (Δ) and equivalence ratio (ϕ). The difference between the equivalence ratio shows an initial discrepancy level of 8% for 0.25cm distance between CFD and PIV. With the increase in distance, the error level increased and for Δ=2cm distance, 15.86% difference has been found. Nonetheless, the CFD results can be improved and error level can be reduced significantly by performing the computation with real injector geometry.

An additional case with injector d2 has been presented also without PIV supported data but it was intended to show that equivalence ratio becomes lower by using a smaller diameter nozzle as it drags more air with high injection velocity (for same inlet condition). Thus the equivalence ratio shifts towards lean condition. The average decrease in equivalence ratio is around 30% while using d2 injector than that of d1. The finding is also supported by Duarte [49] where the similar trend was observed also regarding distance between tube and injector with equivalence ratio.

4.5.2 Comparing equivalence ratio from CFD combustion modeling and corresponding Chemiluminescence Spectroscopy setup

For validating the results between CFD and Chemiluminescence Spectroscopy, a tube with L= 8cm, D=2cm and t=0.25cm has been chosen along with injector d1. In these CFD modelings, the ideal shape was also used for injector. Four inlet mass flow rates, $\dot{v}_{in}$= 0.7, 1, 1.4 and 1.6 SLPM have been selected and the distance Δ was kept at 0.05cm. Practically the injector position was almost at the tube entrance but for modeling purpose a very small gap of 0.05cm is maintained.

The data acquired by spectrometer was processed by a *MATLAB* script. A background test was performed prior to obtaining the main data in 1 second interval for 100 recordings. The processed results show that inlet mass flow rate doesn't necessarily affect the equivalence ratio. The discrepancy between the subsequent readings for each flow rate was limited at 0.8%.
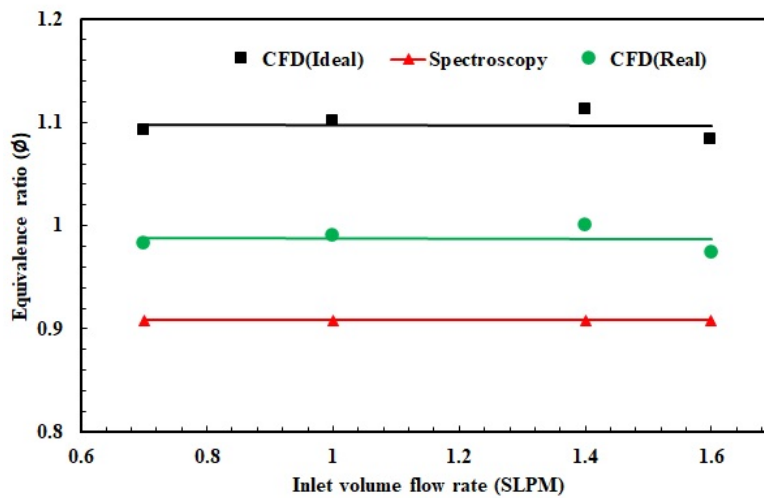

Figure 4.25: Validation of CFD model by observing discrepancy with equivalence ratio values obtained from spectroscopy for a tube L= 8cm, D=2cm and t=0.25cm, injector d1 and $\dot{v}_{in}$= 0.7, 1, 1.4 and 1.6 SLPM.

From Figure 4.25, it is observed that CFD modeling with ideal geometry also shows the similar behavior for the equivalence ratio. As the injection flow rate increases, the equivalence ratio differed from each other only at a level of 2% to 3%. The level of discrepancy between CFD values (ideal) and spectroscopy values varied in between 14% to 18%. As discussed before, modeling with real injector geometry would provide values of equivalence ratio closer to the spectroscopy value. In that case, the primary aeration would increase more due to higher momentum transfer and making the mixture more lean. The same flow conditions were maintained while modeling with the real injector geometry. The CFD results were improved and the level of discrepancy fell down below 10% when comparing to the spectroscopy results. The models support that for a fixed injector position, there's no remarkable change in equivalence ratio. Previous research also suggest similar cases where equivalence ratio is independent of the injection flow rate [49].

Chapter 5

Conclusions and Recommendations

5.1 Present work findings

The main objective in this work was to investigate the air entrainment behavior of an ejector pump premixed firing system and thus estimating equivalence ratio by using CFD as well as two popular non-intrusive diagnostic techniques chemiluminescence spectroscopy and PIV. Different injector geometries have been used both in computational and experimental models along with different size of mixing tubes. Important parameters such as tube diameter (D), injector diameter (d1 and d2), distance between tube and injector (Δ), effect of injection condition $\dot{m}_{in}$, geometric profile of the injectors and their affect have been studied with proper parametric study which establish their strong relationship with the entrainment ratio Rm. The thesis work has always been focused on two particular things: Firstly, to understand and investigate the air entrainment through the mixing tube of the ejector pump burner and secondly, estimating equivalence ratio by using numerical and experimental techniques. Non-intrusive techniques were used to observe the results and later they were compared with the ones from CFD.

Following itemized findings represent the summary of this present work:

- After designing the complete geometry, a proper grid configuration has been developed following a grid independence test and thus setting the total number of elements roughly near 0.2 million considering better result as well as computational cost.

- Two different injector geometries were used in the CFD modeling environment. As the main intention was to determine how entrainment ratio is affected by changing different parameters, for simplicity the numerical models used ideal geometry. By using ideal geometry, it was also intended to investigate the performance of the system and understand its behavior in order to develop a homemade, easy to operate cooking system. For seven different distances (Δ=0.05cm, 0.25 cm, 0.5 cm, 1 cm, 2 cm, 3 cm and 4 cm) and a specific injection mass flow rate and mixing tube, entrainment ratio Rm was always found to be higher using real geometry injector than the ideal one. The discrepancy range varied from 12% to 20% as the distance increases. This is due to higher momentum transfer in real injector that can be visible from the Figure 3.5.

- Lowering the injector diameter gives a higher entrainment ratio as the entrainment velocity is increased due to higher momentum transfer which can be seen comparing the velocity profile for 1mm idea and 0.76mm ideal injector (Appendix A). For the same injection condition an average 29% rise in entrainment ratio is observed.

- The entrainment ratio is slightly changing when the distance (Δ) is maintained in between 0.05 cm to 1 cm. There's a peak condition for the entrainment ratio (for this case 0.5 cm distance) where it was found to be highest. Beyond 2cm, the fall was significant and it was around 15% than the value obtained for 1cm distance. It can be concluded that the operation range of Δ for this specific arrangement needs to be set in between 0.05cm to 1cm.

- If the tube diameter is increased, for the same injection condition, the entrainment ratio starts to rise also for both injectors. Injector d2 exhibits higher entrainment than d1 but for both, there is a limit of tube diameter beyond which the entrainment ratio isn't changing. Though in the beginning the difference was quite significant but when $D = 4$cm, the Rm becomes stable and flat.

- Higher injection condition (mass flow rate or volume flow rate in SLPM) gives higher entrainment ratio. It is valid for both injectors and any tube. But for a specific distance (Δ) and a tube, after a certain value, the increase in entrainment ratio isn't very significant.

- A behavior consistency test has been done by observing the air entrainment found from CFD combustion model and comparing it to the air-air model. it suggests, adding physics for combustion doesn't affect the entrainment behavior which is depending on the parameters (D, d, $\dot{m}_{in}$, Δ) studied before.

- Using the same setup configuration, two models in CFD with and without combustion have been studied to investigate their effects on primary aeration. Cold test gives around 14% more primary aeration than the hot test.

- Using two different injectors (d1, d2) of ideal shape, the equivalence ratio (ϕ) has been estimated from numerical modeling. Due to higher level of entrainment using injector d2, the equivalence ratio for same inlet condition and tube was found to be average 30% lower than the ϕ obtained from d1.

- From the temperature profile developed for a combustion model in CFD environment, nearly the same flame height has been found while comparing to the same experimental setup. The hotter zone remains at the outer section of the flame. The highest temperature was found as 1700K whereas the inner cold region temperature at the beginning was around 310K at middle point of the tube top surface.

- Mass fraction distribution for different chemical species shows their trend during the combustion process. Mass fraction of CO increases with the amount of equivalence ratio thus giving rise to the pollution. More air entrainment causes the CO level to decrease.

- Calibration curves have been generated in order to investigate the equivalence ratio using the ratio of CH^* and C_2^*. It was observed that equivalence ratio remains almost same regardless of the injection mass flow rate while distance (Δ), diameter of tube D, injector diameter d and tube length L remain same. Tube length has also impact on entrainment ratio as increasing L implies and increase of R_m and, therefore a decrease of ϕ.

- PIV analysis shows the level of discrepancy from the CFD ideal and real geometry. It was found the level of discrepancy is reduced while using real injector geometry and shows a close matching to PIV values with an average of 5%.

- Comparison for equivalence ratio between CFD and spectroscopy shows a level of discrepancy from 14% to 18% for the investigated cases. Whereas the PIV and CFD comparison for equivalence ratio shows a difference ranging from 8% to 15% as the distance (Δ) increases. It is expected based on previous findings that real geometry in CFD would give closer values to both non-intrusive diagnostic techniques.

5.2 Recommendations for future work

The developed CFD model was an attempt to represent the actual firing system in a numerical modeling environment. And the diagnostic techniques were used to make a comparison with CFD model. Based on the parametric study, it is observed that they effectively control the lean or rich condition of a flame. As a result, the equivalence ratio as well as the emission control are directly affected.

- Different types of fuels can be used in the same CFD environment developed in this work. Biogas, hydrogen and other fossil fuels or even their mixtures can be investigated through the developed CFD code.

- The same parametric study can be done for different shapes of tubes and injectors. In this study, tube entrance with sharp edge was considered, both in numerical and experimental models. Entrance with round edge or other shapes will affect the air entrainment which is an interesting part of study.

- Heat transfer effect due to conduction and radiation in the tube can be further investigated and their effects of the mixing and entrainment behavior.

- In this developed work, injection flow rates were chosen as a middle value in between flashback and blowoff limits which were experimentally found. The flashback and blowoff phenomena can be visualized and investigated in CFD environment and can be compared with real experimental values.

- Both non-intrusive diagnostic techniques have been proved as a robust tool to investigate equivalence ratio and air entrainment. The scopes can be made broader with the introduction on new injectors, tube and different parametric configurations.

From social engineering perspective, the aforementioned works can provide more in depth information when it comes to the development of clean, convenient and cheap cooking system. For in-lands and rural places, easy and convenient firing system for cooking can be developed based on the guidelines provided in this thesis work. They will not only be informative regarding emission control but also in terms of fuel usage and efficiency of the system.

Bibliography

[1] D. Winterbone and A. Turan. Advanced thermodynamics for engineers. *Butterworth-Heinmann*, ISBN:9780080999838, 2015.

[2] WHO. Fuel for life: household energy and health. *World Health Organization*, 2006.

[3] S. Bonjour, H. Adair-Rohani, J. Wolf, N. Bruce, S. Mehta, A. Prüss-Üstün, M. Lahiff, E. Rehfuess, V. Mishra, and K. Smith. Solid fuel use for household cooking: country and regional estimates for 1980–2010. *Environmental health perspectives*, 121(7):784–790, 2013.

[4] K. Smith, N. Bruce, B. K, H. Adair-Rohani, J. Balmes, Z. Chafe, M. Dherani, H. Hosgood, S. Mehta, D. Pope, and E. Rehfuess. Millions dead: how do we know and what does it mean? methods used in the comparative risk assessment of household air pollution. *Annual review of public health*, 35: 185–206, 2014.

[5] C. Cameron, S. Pachauri, N. Rao, D. McCollum, J. Rogelj, and K. Riahi. Policy trade-offs between climate mitigation and clean cook-stove access in south asia. *Nature Energy*, 1(1):15010, 2016.

[6] M. Bansal, R. Saini, and D. Khatod. Development ofcookingsectorinruralareasinindia—a review. *Renewable and Sustainable Energy Reviews*, 17:44–53, 2013.

[7] T. Lieuwen and B. Zinn. The role of equivalence ratio oscillations in driving combustion instabilities in low nox gas turbines. *Symposium (International) on Combustion*, 27(2):1809–1816, 1998.

[8] S. Turns. An introduction to combustion: Concepts and applications. *McGraw-Hill Education*, ISBN-13:978-0073380193, 2011.

[9] T. Chung, Y. Kim, and J. Sohn. Finite element analysis in combustion phenomena. *International Journal for Numerical Methods in Fluids*, 7:989–1012, 1987.

[10] P. Kumnuan and S. Jugjai. Self-aspirating, liquid fuel, annular porous burner (slapb). *The 5th TSME International Conference on Mechanical Engineering,17-19 December, Chiang Mai, Thailand*, 2014.

[11] P. Muthukumar. Design and development of energy efficient and environment friendly lpg and kerosene cooking stoves with porous radiant burners for household and large-scale cooking applications. *Project 6727, Impacting Research Innovation and Technology (IMPRINT-India)*, 2017.

[12] A. Namkhat and S. Jugjai. Primary air entrainment characteristics for a self-aspirating burner: Model and experiments. *Energy*, 35:1701–1708, 2010.

[13] R. Pritchard, J. Guya, and N. Connor. Handbook of industrial gas utilization:engineering principles and practice. *New York: Van Nostrand Reinhold Co.*, ISBN-13: 978-0442266356, 1977.

[14] G. Singh, T. Sundararajan, and U. Shet. Entrainment and mixing studies for a variable density confined jet. *Numerical Heat Transfer, Part A: Applications*, 35(2):205–223, 1999.

[15] G. Singh, T. Sundararajan, and K. Bhaskaran. Mixing and entrainment characteristics of circular and noncircular confined jets. *Journal of Fluids Engineering*, 125:835–842, 2003.

[16] A. Almeida, R. Laranjeira, L. Monteiro, A. Santos, and E. Fernandes. 1d model for a low nox ejector-pump like burner. *Experimental Thermal and Fluid Science*, 100:171–192, 2019.

[17] P. Boggavarapu, B. Ray, and R. Ravikrishna. Thermal efficiency of lpg and png-fired burners: Experimental and numerical studies. *Fuel*, 116:709–715, 2014.

[18] Z. Wei, X. Li, L. Xu, and T. C. Optimization of operating parameters for low nox emission in high-temperature air combustion. *Energy Fuels*, 26(5):2821–2829, 2012.

[19] U. Kesgin. Study on prediction of the effects of design and operating parameters on nox emissions form a lean burn natural gas engine. *Energy Conversion and Management*, 44(4):907–921, 2003.

[20] F. Liu, X. You, Q. Wang, and R. Zhang. On optimal design and experimental validation of household appliance burner of low pollutant emission. *Energy Conversion and Management*, 76:837–845, 2013.

[21] N. Docquier and S. Candel. Combustion control and sensors: a review. *Progress in Energy and Combustion Science*, 28(2):107–150, 2002.

[22] C. Lawn. A simple method for the design of gas burner injectors. *Proceedings of the Institution of Mechanical Engineers, Part C: Journal of Mechanical Engineering Science*, 217(2):237–246, 2003.

[23] K. Sutar, M. Ravi, and S. Kohli. Design of a partially aerated naturally aspirated burner for producer gas. *Energy*, 116:773–785, 2016.

[24] H. Jones. The application of combustion principles to domestic gas burner design. *Taylor Francis*, ISBN 13:9780419148005, 1989.

[25] A. Hemidi, F. Henry, S. Leclaire, J. Seynhaeve, and Y. Bartosiewicz. Cfd analysis of a supersonic air ejector. part i: Experimental validation of single-phase and two-phase operation. *Applied Thermal Engineering*, 29:1523–1531, 2009.

[26] K. Pianthong, W. Seehanam, M. Behnia, T. Sriveerakul, and S. Aphornratana. Investigation and improvement of ejector refrigeration system using computational fluid dynamics technique. *Energy Conversion and Management*, 48:2556–2564, 2007.

[27] D. Zhao, F. Liu, X. You, R. Zhang, B. Zhang, and G. He. Optimization of a premixed cylindrical burner for low pollutant emission. *Energy Conversion and Management*, 99:151–160, 2015.

[28] Y. Sommerer, D. Galley, T. Poinsot, S. Ducruix, F. Lacas, and D. Veynante. Large eddy simulation and experimental study of flashback and blow-off in a lean partially premixed swirled burner. *Journal of Turbulence*, 5(37):1–21, 2004.

[29] Y. Hardalupas and M. Orain. Local measurements of the time-dependent heat release rate and equivalence ratio using chemiluminescent emission from a flame. *Combustion and Flame*, 139:188–207, 2004.

[30] A. Boateng. Rotary kilns:transport phenomena and transport processes. *Butterworth-Heinemann*, ISBN: 9780080557120, 2008.

[31] R. Vichnevetsk. Computer methods for partial differential equations. *Prentice Hall, Englewood Cliffs, NJ*, ISBN 13:9780131652330, 1981.

[32] T. Echekki and E. Mastorakos. Turbulent combustion modeling: Advances, new trends and perspectives. *Springer*, ISBN:978-94-007-0412-1, 2011.

[33] C. Argyropoulos and N. Markatos. Recent advances on the numerical modelling of turbulent flows. *Applied Mathematical Modelling*, 39(2):693–732, 2015.

[34] A. Kolmogorov. Equations of turbulent motion of an incompressible fluid. *Izv. Acad. Nauk USSR*, 6:56–58, 1942.

[35] D. Spalding. Mathematical models of turbulent transport processes. *Imperial College of Science and Technology, Department of Mechanical Engineering*, 1978.

[36] D. Wilcox. Formulation of the kw turbulence model revisited. *AIAA journal*, 46(11):2823–2838, 2008.

[37] T. Poinsot and D. Veynante. Theoretical and numerical combustion. *R.T. Edwards, Inc.*, ISBN-13: 978-1930217102, 2005.

[38] D. Spalding. Concentration fluctuations in a round turbulent free jet. *Chemical Engineering Science*, 26(1):95–107, 1971.

[39] T. Li, C. Armstrong, and R. McKeag. Quad mesh generation for k-sided faces and hex mesh generation for trivalent polyhedra. *Finite Element Analysis and Design*, 26:271–301, 1997.

[40] A. Gaydon and H. Wolfhard. Flames, their structure, radiation, and temperature. *Springer US*, 978-1-5041-2585-7, 1960.

[41] T. Trindade, A. Ferreira, and E. Fernandes. Characterization of combustion chemiluminescence: an image processing approach. *Procedia Technology*, 17:194–201, 2014.

[42] J. Kojima, Y. Ikeda, and T. Nakajima. Spatially resolved measurement of OH^*, CH^* and C_2^* chemiluminescence in the reaction zone of laminar methane/air premixed flames. *Proceedings of the Combustion Institute*, 28(2):1757–1764, 2000.

[43] H. Itoh, Y. Hommo, K. Noda, and T. Gomi. Instantaneous measuring method of air–fuel ratio by luminous intensity of radicals. *Jidousha Gijyutsukai Ronbunshu*, 29:10–17, 1984.

[44] H. Itoh, Y. Hommo, J. Song, and T. Gomi. An instantaneous measuring method of air–fuel ratio by luminous intensity of radicals (applications to practical burner flames). *JSME Transactions B*, 52: 3362–3371, 1986.

[45] K. Okamoto, S. Nishio, T. Saga, and T. Kobayashi. Standard images for particle-image velocimetry. *Measurement Science and Technology*, 11(6):685–691, 2000.

[46] M. Raffel, C. Willert, S. Wereley, and J. Kompenhans. Particle image velocimetry: A practical guide. *Springer-Verlag Berlin Heidelberg*, ISBN:978-3-540-72308-0, 2007.

[47] R. Lindken and S. Burgmann. Laser-optical methods for transport studies in low temperature fuel cells. *Polymer Electrolyte Membrane and Direct Methanol Fuel Cell Technology*, ISBN-13: 978-1845697747:425–461, 2012.

[48] Y. Zhu, W. Cai, C. Wen, and Y. Li. Numerical investigation of geometry parameters for design of high performance ejectors. *Applied Thermal Engineering*, 29(5-6):898–905, 2009.

[49] G. Duarte. Improvement of the stable limits and primary air entrainment in a single burner of a domestic water heater unit. *Doctoral dissertation, MSc Thesis, Instituto Superior Técnico*, 2008.

[50] J. Jarosinski and B. Veyssiere. Combustion phenomena: Selected mechanisms of flame formation, propagation and extinction. *CRC Press*, ISBN:9781138113886, 2017.

[51] S. Tieng, W. Lai, and T. Fujiwara. Holographic temperature measurement on axisymmetric propane-air, fuel-lean flame. *Measurement Science and Technology*, 3:1179–1187, 1992.

[52] M. Ishak and M. Jaafar. The influence of orifice insertion in radial swirling flow for low emissions combustion. *Jurnal Mekanikal*, 26:96–106, 2008.

[53] R. Wang, L. Yongping, and S. Yaowu. Numerical simulation of transient temperature field during laser keyhole welding of 304 stainless steel sheet. *Optics Laser Technology*, 43(4):870–873, 2011.

[54] R. Bastiaans. Cross-correlation piv; theory, implementation and accuracy. *Eindhoven University of Technology, Faculty of Mechanical Engineering*, 2000.

[55] A. Sciacchitano. Uncertainty quantification in particle image velocimetry. *Measurement Science and Technology*, 30:092001, 2019.

Appendix A

Flame profiles

(a) Flame profile for Δ=0.25cm

(b) Flame profile for Δ=0.5cm

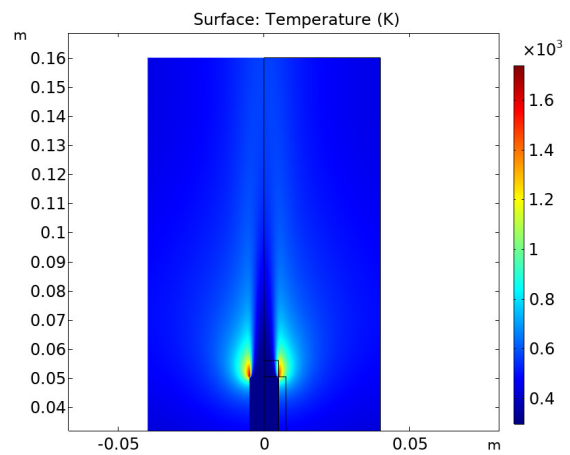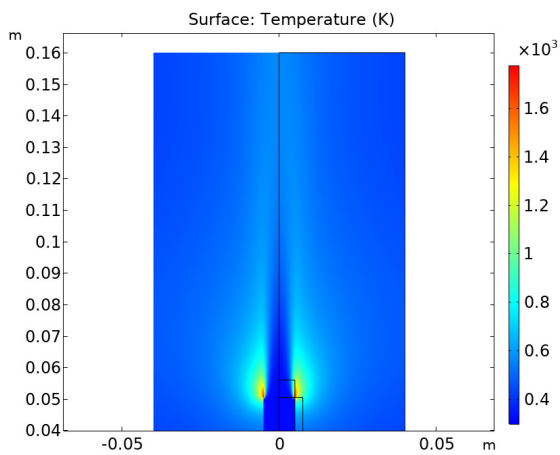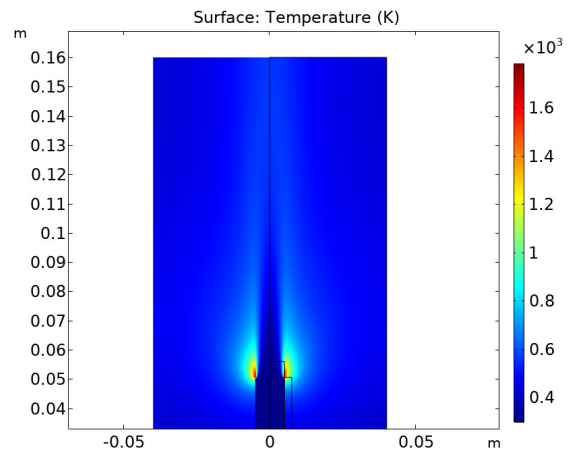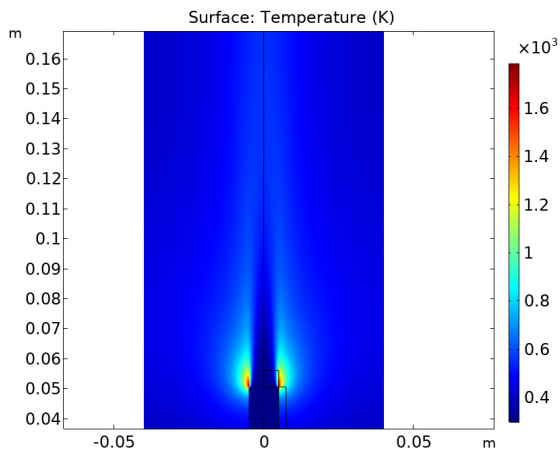(c) Flame profile for Δ=1cm

(d) Flame profile for Δ=2cm

Figure A.1: Flame temperature profile modeled in CFD environment for an inlet condition of 0.806 SLPM, tube T2, injector d1 and Δ=0.25cm, 0.5cm, 1cm and 2cm .
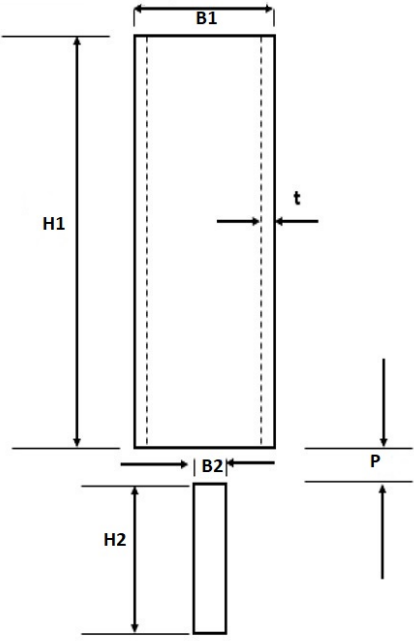
Appendix B

Drawings

Figure B.1: Parameterized drawing of the setup in COMSOL modeling environment.